

## Article

# Impedance Modeling and Stability Analysis of Three-Phase Four-Wire Inverter with Grid-Connected Operation

Guoli Feng, Zhihao Ye, Yihui Xia \*, Liming Huang and Zerun Wang

College of Electrical Engineering, Navel University of Engineering, JieFang Road 717, Wuhan 430000, China; fengguoli80@163.com (G.F.); yxyx926@126.com (Z.Y.); huangliming1998@163.com (L.H.); wzrunfly@163.com (Z.W.)

\* Correspondence: xiayihui2005@163.com

**Abstract:** With the continuous penetration and development of renewable energy power generation, distributed grids and microgrids are becoming increasingly important in power systems. In the distribution networks and microgrids, the grid impedance is comparatively large and cannot be ignored. Usually, the parallel compensation is used to improve the grid quality. In these three-phase four-wire power systems, analyzing the impedance characteristics of the grid-connected inverter is vital to carry out the small-signal stability analysis. Thus, it is vital to consider the influence of the zero-sequence component in addition to the positive-sequence component and the negative-sequence component when it comes to analyzing system stability. In this paper, the impedances of three-phase four-wire split capacitor inverter and three-phase four-leg inverter are established. Based on the achieved impedance, the similarities and differences between the impedances of three-phase four-wire split capacitor inverter and impedance of three-phase four-leg inverter are studied. The main difference is reflected in zero-sequence impedance. Additionally, the zero-sequence impedance characteristics and the dominating factors deciding the zero-sequence impedance are analyzed. Then, the stability of the system considering the grid impedance and impedance of three-phase four-wire inverter is investigated by separately considering the stability of the positive–negative-sequence component and the stability of the zero-sequence component. Several cases of small-signal instability caused by the positive–negative-sequence component or zero-sequence component are revealed. The experimental results validate the theoretical analysis.

**Keywords:** three-phase four-wire inverter; impedance modeling; stability



**Citation:** Feng, G.; Ye, Z.; Xia, Y.; Huang, L.; Wang, Z. Impedance Modeling and Stability Analysis of Three-Phase Four-Wire Inverter with Grid-Connected Operation. *Energies* **2022**, *15*, 2754. <https://doi.org/10.3390/en15082754>

Academic Editor: Nicu Bizon

Received: 11 February 2022

Accepted: 2 April 2022

Published: 8 April 2022

**Publisher's Note:** MDPI stays neutral with regard to jurisdictional claims in published maps and institutional affiliations.



**Copyright:** © 2022 by the authors. Licensee MDPI, Basel, Switzerland. This article is an open access article distributed under the terms and conditions of the Creative Commons Attribution (CC BY) license (<https://creativecommons.org/licenses/by/4.0/>).

## 1. Introduction

With the continuous penetration and development of renewable energy power generation, distribution networks and microgrids account for an increasing proportion of contemporary power grids [1–3]. In distribution networks and microgrids, the three-phase four-wire system has been widely promoted and applied [4–9], because it can provide a zero-sequence current path and is suitable for both symmetrical and asymmetrical conditions. In the three-phase four-wire system, the three-phase four-wire inverter has important functions such as power transmission and power quality improvement devices. The three-phase four-wire split capacitor inverter (TFSCI) and three-phase four-leg inverter (TFGI) have been widely used due to their low cost, simple control, and small size. Their application scenarios include islanded microgrid [4], active filter [5], power redistribution device [6], renewable energy power generation system [7], uninterruptible power supply [8], and power distribution system [9].

Because the distribution network and microgrid are usually weak grids with large impedance, parallel compensation capacitors are typically equipped to perform reactive power compensation and harmonic filtering to improve voltage quality and enlarge power transmission capacity [10–12]. Therefore, it is a very common scenario in a three-phase

four-wire system that the three-phase four-wire inverter connects to a weak grid with parallel compensation capacitors.

When the three-phase four-wire inverter connects to the grid whose impedance cannot be neglected, the interactions between the inverter systems and weak grid may cause stability issues. Many methods can be used to analyze the characteristics of system stability. These methods include the loop-gain method [13–15], eigenvalues analysis based on system state-space method [16], the passivity method [17,18], and the impedance-based method [19–25].

Among these analytical methods, the impedance-based analysis method is proved as an effective way to study and resolve the small-signal instability problems caused by the interaction between the converter and the grid [21–25]. A stability criterion for grid-connected inverters based on Gershgorin's theorem and impedance model is proposed in [21]. Reference [22] establishes the entire impedance of RSC and VSC considering coupling factors to analyze the system stability. In [23], a single-in-single-out impedance model of grid-connected inverters with a virtual synchronous generator using a cascaded inner control loop is established to analyze the system stability under different kinds of weak grids.

The small-signal instability problems of the three-phase three-wire grid-connected inverter system have received wide attention and research, and numerous meaningful conclusions have been achieved. However, these conclusions cannot accurately reflect the stability of three-phase four-wire grid-connected inverter system because the zero-sequence component is not considered. The zero-sequence component is also a factor that will cause the small-signal instability of the system except the negative-sequence and the positive-sequence components.

To analyze the small-signal stability of the three-phase four-wire system including zero-sequence stability by the analysis method based on impedance, the impedance of the three-phase four-wire inverter should be achieved firstly. By analyzing the transmission path of the zero-sequence, positive-sequence, and negative-sequence small-signals perturbation in each sequence loop considering all the control blocks, the relationship between the small signal perturbation and the corresponding response in the frequency domain will be achieved as an impedance model of the inverter.

The derivation process of the impedance model including the zero-sequence impedance, positive-sequence impedance, and negative-sequence impedance is much more complex than that of the three-phase three-wire inverter impedance model. The matrix dimension increases from two-dimensional to three-dimensional, and the effect of the zero-sequence component on the disturbance loop should be considered. Then, the small-signal instability issue can be studied on the basis of the obtained impedance model. When performing stability analysis, it is not only necessary to consider the stability of the positive and negative sequences, but also to consider whether the zero-sequence impedance will bring stability problems, which increases the complexity of the analysis process.

Additionally, based on the obtained impedance model, the impedance characteristics of TFSCI and TFGI are analyzed in this paper. The small-signal stability of TFSCI and TFGI are analyzed, and the instability cases are given in the weak grid and weak grid with parallel compensation.

The structure of the paper is organized as follows. Section 2 gives the system description and impedance models of TFSCI and TFGI. Then, the comparison of impedance characteristics between TFSCI and TFGI is presented in Section 3. The stability analyses of TFSCI and TFGI are studied in Section 4. The validity of the established impedance and stability analysis method are verified by experiments in Section 5. Section 6 concludes this paper.

## 2. System Description and Impedance Modeling of TFSCI and TFGI

### 2.1. Impedance Modeling of TFSCI

The block diagram of TFSCI connected to the parallel compensation grid is shown in Figure 1. In Figure 1,  $L_{fa}$ ,  $L_{fb}$ ,  $L_{fc}$ , and  $L_{fn}$  represent the filter inductors;  $R_{fa}$ ,  $R_{fb}$ ,  $R_{fc}$ , and

$R_{fn}$  represent corresponding parasitic resistances.  $C_1$  and  $C_2$  are the DC-side capacitors, where  $C_1 = C_2 = C_{dc}$ . In Figure 1, the SRF-PLL is the synchronous reference frame phase-locked loop to achieve the synchronous angle of the grid. Based on the achieved angle, the currents and voltage in the  $dq0$ -domain can be obtained by the Park transformation. The PI controllers  $PI_d$ ,  $PI_q$ , and  $PI_0$  are used to control the  $d$ -axis,  $q$ -axis, and 0-axis currents, respectively. The PI controller  $PI_{DC}$  is used to balance the DC voltage of  $C_1$  and  $C_2$ .

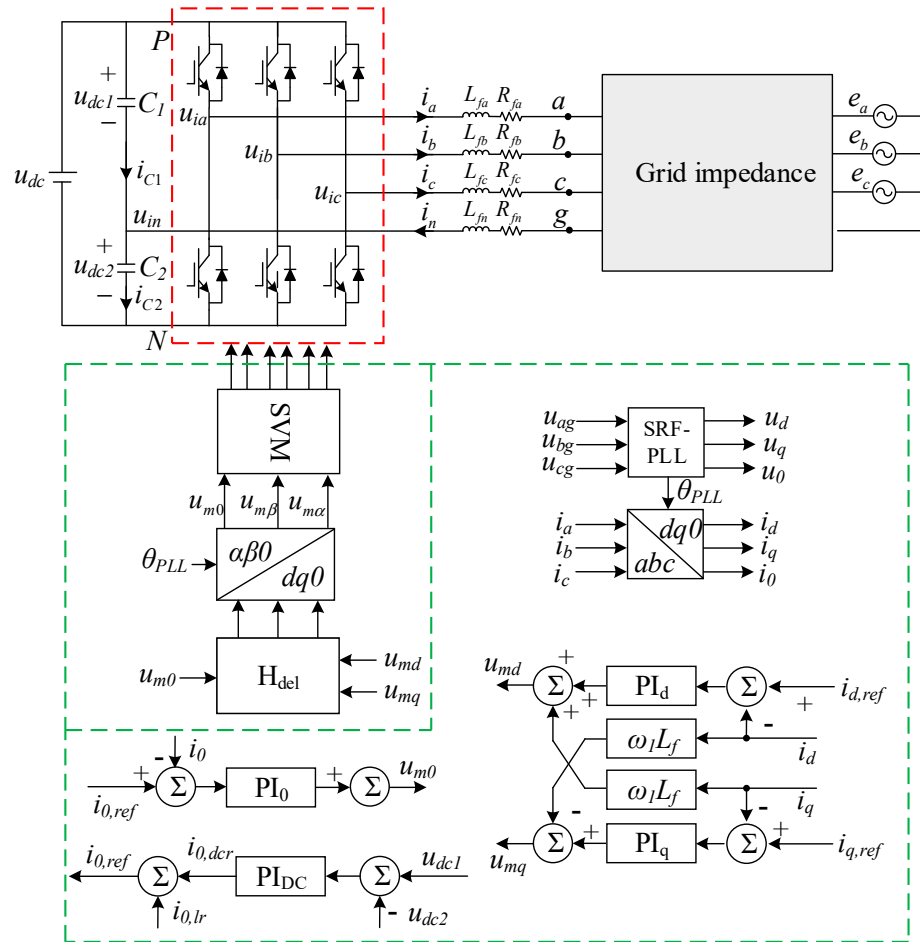


Figure 1. Block diagram of TFSCI.

The voltages in each leg of the TFSCI, measured from the negative point of the DC-link  $N$ , can be obtained as,

$$\begin{bmatrix} u_{aN} \\ u_{bN} \\ u_{cN} \end{bmatrix} = \begin{bmatrix} S_a \\ S_b \\ S_c \end{bmatrix} u_{dc} \tag{1}$$

where  $S_a$ ,  $S_b$ , and  $S_c$  are the signals used to control the switching states.

According to (1), the phase voltage can be expressed as,

$$\begin{bmatrix} u_{an} \\ u_{bn} \\ u_{cn} \end{bmatrix} = \begin{bmatrix} u_{aN} - u_{nN} \\ u_{bN} - u_{nN} \\ u_{cN} - u_{nN} \end{bmatrix} - \begin{bmatrix} u_{dc2} \\ u_{dc2} \\ u_{dc2} \end{bmatrix} = \begin{bmatrix} d_a \\ d_b \\ d_c \end{bmatrix} u_{dc} - \begin{bmatrix} u_{dc2} \\ u_{dc2} \\ u_{dc2} \end{bmatrix} \tag{2}$$

where  $d_a$ ,  $d_b$ ,  $d_c$  are the duty ratios of phase a, phase b, and phase c, respectively.

From Figure 1, under the assumption that  $L_{fa} = L_{fb} = L_{fc} = L_f$ ,  $R_{fa} = R_{fb} = R_{fc} = R_f$ ,  $L_{fn} = L_n$ ,  $R_{fn} = R_n$ , through Kirchhoff's voltage law, the voltages in the three-phase domain can be written as,

$$\begin{bmatrix} u_{an} \\ u_{bn} \\ u_{cn} \end{bmatrix} = \begin{bmatrix} L_{fa} & 0 & 0 \\ 0 & L_{fb} & 0 \\ 0 & 0 & L_{fc} \end{bmatrix} \begin{bmatrix} pi_a \\ pi_b \\ pi_c \end{bmatrix} + \begin{bmatrix} R_{fa} & 0 & 0 \\ 0 & R_{fb} & 0 \\ 0 & 0 & R_{fc} \end{bmatrix} \begin{bmatrix} i_a \\ i_b \\ i_c \end{bmatrix} + L_{fn} \begin{bmatrix} pi_n \\ pi_n \\ pi_n \end{bmatrix} + R_{fn} \begin{bmatrix} i_n \\ i_n \\ i_n \end{bmatrix} + \begin{bmatrix} u_{ag} \\ u_{bg} \\ u_{cg} \end{bmatrix} \quad (3)$$

where  $p$  represents the differential operator  $d/dt$ .

Through Kirchhoff’s current law, the zero-sequence current can be written as,

$$i_0 = \frac{C_f}{3} \frac{d(u_{c2} - u_{c1})}{dt} \quad (4)$$

Practically, the circuit model is usually converted to the  $dq0$  coordinate system to achieve decoupling control of active and reactive currents. The synchronous reference frame phase-locked loop (SRF-PLL) is extensively used to obtain the coordinate transformation angle  $\theta$  between the three-phase frames and the  $dq0$  frames. The block diagram of SRF-PLL is shown in Figure 2.

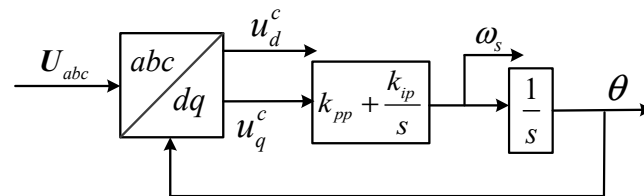


Figure 2. Block diagram of PLL.

Then, with joints (2) and (3), through the Park transformation, the mathematical model in the system  $dq0$  frame can be obtained as,

$$\begin{bmatrix} d_d \\ d_q \\ d_0 \end{bmatrix} u_{dc} = \begin{bmatrix} L_f & 0 & 0 \\ 0 & L_f & 0 \\ 0 & 0 & 3L_n + L_f \end{bmatrix} \begin{bmatrix} pi_d \\ pi_q \\ pi_0 \end{bmatrix} + \begin{bmatrix} R_f & 0 & 0 \\ 0 & R_f & 0 \\ 0 & 0 & 3R_n + R_f \end{bmatrix} \begin{bmatrix} i_d \\ i_q \\ i_0 \end{bmatrix} + \begin{bmatrix} 0 & \omega L_f & 0 \\ -\omega L_f & 0 & 0 \\ 0 & 0 & 0 \end{bmatrix} \begin{bmatrix} i_d \\ i_q \\ i_0 \end{bmatrix} + \begin{bmatrix} u_d \\ u_q \\ u_0 \end{bmatrix} - \begin{bmatrix} 0 \\ 0 \\ u_{dc2} \end{bmatrix} \quad (5)$$

In Equation (5),  $p$  is the differential operator  $d/dt$ .

From Figure 3, assuming  $\Delta d_d^s = \Delta d_q^s = \Delta d_0^s$ , the transfer function matrix from perturbation voltage to current response in the system frame can be expressed as,

$$\mathbf{Z}_{SCout} = \begin{bmatrix} sL_f + R_f & \omega L_f & 0 \\ -\omega L_f & sL_f + R_f & 0 \\ 0 & 0 & s(L_f + 3L_n) + R_f + 3R_n - \frac{3}{2sC} \end{bmatrix} \quad (6)$$

The ‘ $s$ ’ represents the Laplace operator in Equation (6). The detailed derivation process can be seen in Appendix A.

The small-signal model from (5) can be derived. Figure 4 shows its equivalent circuit in which  $X$  is the steady-state value of  $X$ , and  $\Delta x$  represents the small-signal perturbation. Note that the small-signal model is established on the quiescent operation point.

Similarly, in Figure 3, assuming  $\Delta u_d^s = \Delta u_q^s = \Delta u_0^s = 0$ , the transfer function matrix from duty ratio perturbation to the corresponding current response can be expressed as,

$$\mathbf{H}_{SCid} = \begin{bmatrix} \frac{-(sL_f + R_f)U_{dc}}{(sL_f + R_f)^2 + (\omega L_f)^2} & \frac{\omega L_f U_{dc}}{(sL_f + R_f)^2 + (\omega L_f)^2} & 0 \\ -\frac{\omega L_f U_{dc}}{(sL_f + R_f)^2 + (\omega L_f)^2} & \frac{-(sL_f + R_f)U_{dc}}{(sL_f + R_f)^2 + (\omega L_f)^2} & 0 \\ 0 & 0 & \frac{-U_{dc}}{s(3L_n + L_f) + 3R_n + R_f - \frac{3}{2sC}} \end{bmatrix} \quad (7)$$

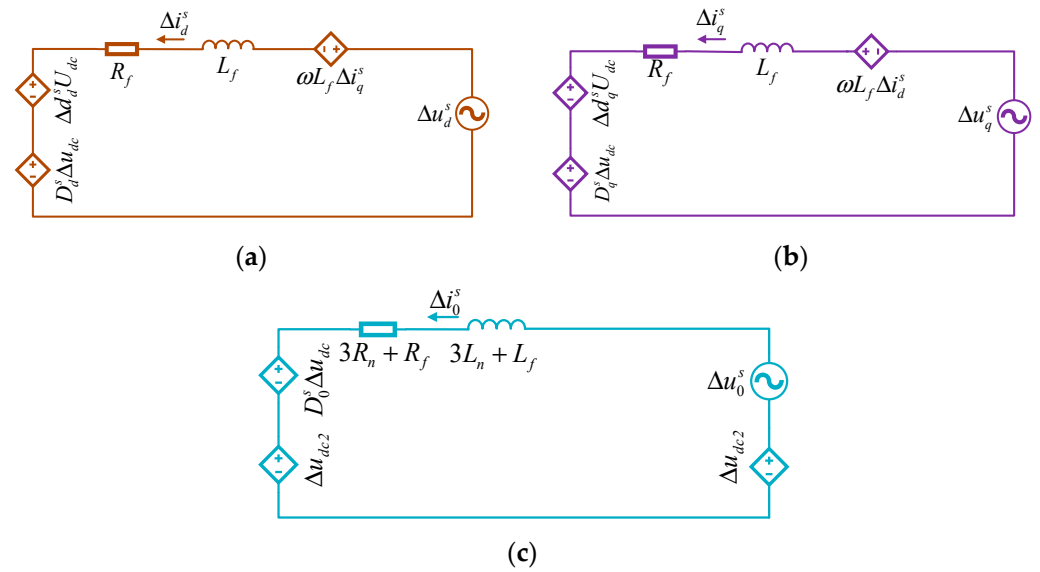


Figure 3. Small-signal circuit model of TFSCI. (a) Small-signal circuit in  $d$ -axis; (b) small-signal circuit in  $q$ -axis; (c) small-signal circuit in  $0$ -axis.

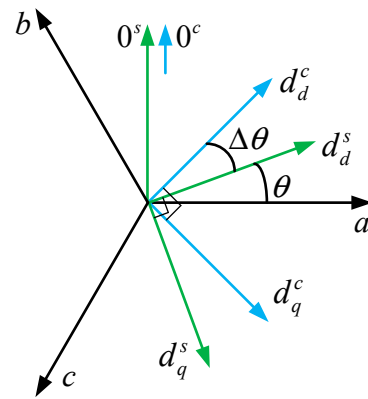


Figure 4. Relationship between controller frame and system frame.

Because of the dynamic performance of SRF-PLL, harmonic voltages will bring about corresponding phase perturbation, leading to an angular difference  $\Delta\theta$  between the controller  $dq0dq0$  frame and system  $dq0dq0$  frame in the  $d$ -axis and  $q$ -axis except  $0$ -axis. In this paper, the variable in the controller  $dq0dq0$  frame is defined as  $X^c$  with superscript  $c$  while  $X^s$  with superscript  $s$  is in the system  $dq0$  frame. The relationship between the controller and system  $dq0$  frames can be seen in Figure 4.

From Figure 2,  $\Delta\theta$  can be obtained as,

$$\Delta\theta = \Delta u_q^c \left( k_{pp} + \frac{k_{ip}}{s} \right) \frac{1}{s} \tag{8}$$

The conversion of the variables in the system  $dq0$ -domain to the controller  $dq0$ -domain can be obtained as,

$$\vec{X}^c = \begin{bmatrix} \cos(\Delta\theta) & -\sin(\Delta\theta) & 0 \\ \sin(\Delta\theta) & \cos(\Delta\theta) & 0 \\ 0 & 0 & 1 \end{bmatrix} \vec{X}^s \tag{9}$$

Introducing the perturbation, the relationships between  $\vec{U}$  and  $\vec{U}^s$ , and  $\vec{I}$  and  $\vec{I}^s$  in the small-signal model can be expressed as:

$$\begin{bmatrix} U_d^c + \Delta u_d^c \\ U_q^c + \Delta u_q^c \\ U_0^c + \Delta u_0^c \end{bmatrix} = \begin{bmatrix} \cos(\Delta\theta) & -\sin(\Delta\theta) & 0 \\ \sin(\Delta\theta) & \cos(\Delta\theta) & 0 \\ 0 & 0 & 1 \end{bmatrix} \begin{bmatrix} U_d^s + \Delta u_d^s \\ U_q^s + \Delta u_q^s \\ U_0^s + \Delta u_0^s \end{bmatrix} \tag{10}$$

$$\begin{bmatrix} I_d^c + \Delta i_d^c \\ I_q^c + \Delta i_q^c \\ I_0^c + \Delta i_0^c \end{bmatrix} = \begin{bmatrix} \cos(\Delta\theta) & -\sin(\Delta\theta) & 0 \\ \sin(\Delta\theta) & \cos(\Delta\theta) & 0 \\ 0 & 0 & 1 \end{bmatrix} \begin{bmatrix} I_d^s + \Delta i_d^s \\ I_q^s + \Delta i_q^s \\ I_0^s + \Delta i_0^s \end{bmatrix} \tag{11}$$

The  $\Delta\theta$  is ignorable; then, (10) and (11) can be simplified as,

$$\begin{bmatrix} \Delta u_d^c \\ \Delta u_q^c \\ \Delta u_0^c \end{bmatrix} \approx \begin{bmatrix} \Delta u_d^s + U_q^s \Delta\theta \\ \Delta u_q^s - U_d^s \Delta\theta \\ \Delta u_0^s \end{bmatrix} \tag{12}$$

$$\begin{bmatrix} \Delta i_d^c \\ \Delta i_q^c \\ \Delta i_0^c \end{bmatrix} \approx \begin{bmatrix} \Delta i_d^s + I_q^s \Delta\theta \\ \Delta i_q^s - I_d^s \Delta\theta \\ \Delta i_0^s \end{bmatrix} \tag{13}$$

Combining (8) and (10), the relationship between  $\Delta\theta$  and  $\Delta u_q^s$  can be expressed as,

$$\Delta\theta = \frac{k_{pp} + k_{pi}/s}{s + U_d^s * (k_{pp} + k_{pi}/s)} \Delta u_q^s \tag{14}$$

Defining

$$H_{PLL} = \frac{k_{pp} + k_{ip}/s}{s + U_d^s * (k_{pp} + k_{ip}/s)} \tag{15}$$

Joining (12) to (11), the relationship between  $\Delta u^s$  can  $\Delta i^c$  be obtained as,

$$\begin{bmatrix} \Delta i_d^c \\ \Delta i_q^c \\ \Delta i_0^c \end{bmatrix} = \begin{bmatrix} 0 & I_q^s H_{PLL} & 0 \\ 0 & -I_d^s H_{PLL} & 0 \\ 0 & 0 & 0 \end{bmatrix} * \begin{bmatrix} \Delta u_d^s \\ \Delta u_q^s \\ \Delta u_0^s \end{bmatrix} \tag{16}$$

Defining  $\mathbf{H}_{PLL}^i$  as the matrix of  $\Delta u^s$  to  $\Delta i^c$ ,

$$\mathbf{H}_{PLL}^i = \begin{bmatrix} 0 & H_{PLL} I_q^s & 0 \\ 0 & -H_{PLL} I_d^s & 0 \\ 0 & 0 & 0 \end{bmatrix} \tag{17}$$

Similarly, the matrix  $\mathbf{H}_{PLL}^d$  of  $\Delta u^s$  to duty ratio perturbation can be obtained as,

$$\mathbf{H}_{PLL}^d = \begin{bmatrix} 0 & -D_q^s H_{PLL} & 0 \\ 0 & D_q^s H_{PLL} & 0 \\ 0 & 0 & 0 \end{bmatrix} \tag{18}$$

The control block diagram, mainly including the DC voltage balance PI controller, the PLL, and the current PI controller, makes a great contribution to the performance of the system, which is necessary to be considered in the modeling process.

The block diagram of the impedance model of TFSCI can be seen in Figure 5. Matrix  $\mathbf{H}_{del}$  represents the control delay element, matrix  $\mathbf{H}_{dec}$  represents the  $d$ - $q$  decoupling term in the current controller, and matrix  $\mathbf{H}_{ci}$  represents the PI regulator in the current controller.

$$\mathbf{H}_{dec} = \begin{bmatrix} 0 & -\omega L_f & 0 \\ \omega L_f & 0 & 0 \\ 0 & 0 & 0 \end{bmatrix} \tag{19}$$

$$\mathbf{H}_{dc} = \begin{bmatrix} 1/U_{dc} & 0 & 0 \\ 0 & 1/U_{dc} & 0 \\ 0 & 0 & 1/U_{dc} \end{bmatrix} \tag{20}$$

$$\mathbf{H}_{del} = \begin{bmatrix} e^{-T_{del}s} & 0 & 0 \\ 0 & e^{-T_{del}s} & 0 \\ 0 & 0 & e^{-T_{del}s} \end{bmatrix} \tag{21}$$

$$\mathbf{H}_{ci} = \begin{bmatrix} k_{dip} + \frac{k_{dii}}{s} & 0 & 0 \\ 0 & k_{qip} + \frac{k_{qii}}{s} & 0 \\ 0 & 0 & k_{0ip} + \frac{k_{0ii}}{s} \end{bmatrix} \tag{22}$$

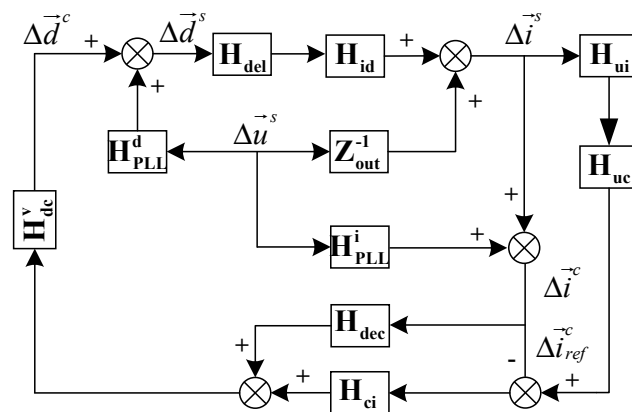


Figure 5. The impedance model block diagram of TFSCI.

From (4), matrix  $\mathbf{H}_{ui}$  of the perturbation of current in the system  $dq0$  frame to the perturbation of DC voltage can be expressed as,

$$\mathbf{H}_{ui} = \begin{bmatrix} 0 & 0 & 0 \\ 0 & 0 & 0 \\ 0 & 0 & -3/2SC_f \end{bmatrix} \tag{23}$$

From Figure 1, in the DC voltage balance PI controller, the expression  $\mathbf{G}_{cu}$  from the perturbation of DC voltage to the perturbation current reference can be obtained as,

$$\mathbf{G}_{cu} = \begin{bmatrix} 0 & 0 & 0 \\ 0 & 0 & 0 \\ 0 & 0 & k_{dcp} + k_{dci}/s \end{bmatrix} \tag{24}$$

According to Figure 5, the admittance from  $\Delta i^{\rightarrow s}$  to  $\Delta u^{\rightarrow s}$ , or the admittance of TFSCI in the  $dq0$ -domian, can be obtained as,

$$\mathbf{Y}_{SCdq0} = \frac{\mathbf{H}_{SCid}\mathbf{H}_{del}\mathbf{H}_{dc}(\mathbf{H}_{PLL}^i(\mathbf{H}_{dec}-\mathbf{H}_{ci})) + \mathbf{H}_{SCid}\mathbf{H}_{del}(\mathbf{H}_{PLL}^d + (\mathbf{H}_{SCid}\mathbf{H}_{del})^{-1}\mathbf{Z}_{out}^{-1})}{\mathbf{I} - \mathbf{H}_{SCid}\mathbf{H}_{del}\mathbf{H}_{dc}(\mathbf{H}_{dec}-\mathbf{H}_{ci}) - \mathbf{G}_{cu}\mathbf{H}_{ci}\mathbf{H}_{dc}\mathbf{H}_{ui}\mathbf{H}_{SCid}\mathbf{H}_{del}} \tag{25}$$

In the actual system, the components in the  $pn0$ -domain are easier to measure than the components in the  $dq0$ -domain. Therefore, it is necessary to transform the impedances in the  $dq0$ -domain to the impedances in the  $pn0$ -domain. In the case of three-phase symmetrical conditions, reference [26] indicates that the admittance in the  $dq0$ -domain can be equivalently transformed into the sequence domain as,

$$Y_{SCpn0} = T_Z Y_{dq0} T_Z^{-1} = \begin{bmatrix} Y_{ipn} & 0 \\ 0 & Y_{i0} \end{bmatrix} = \begin{bmatrix} Y_{11} & Y_{12} & 0 \\ Y_{21} & Y_{22} & 0 \\ 0 & 0 & Y_{33} \end{bmatrix} \tag{26}$$

$$T_Z = \frac{1}{\sqrt{2}} \begin{bmatrix} 1 & j & 0 \\ 1 & -j & 0 \\ 0 & 0 & \sqrt{2} \end{bmatrix} \tag{27}$$

### 2.2. Impedance Modeling of the TFGI

The block diagram of the TFGI connected to the parallel compensation grid is shown in Figure 6. In Figure 1,  $L_f$  and  $L_n$  represent the filter inductor, and  $R_f$  and  $R_{fn}$  represent the corresponding parasitic resistance. Referring to the derivation process in Section 2.1, the admittance of TFGI in the  $dq0$ -domain can be expressed as [27],

$$Y_{FLpn0} = T_Z Y_{dq0} T_Z^{-1} = \begin{bmatrix} Y_{ipn} & 0 \\ 0 & Y_{i0} \end{bmatrix} = \begin{bmatrix} Y_{11} & Y_{12} & 0 \\ Y_{21} & Y_{22} & 0 \\ 0 & 0 & Y_{33} \end{bmatrix} \tag{28}$$

$$T_Z = \frac{1}{\sqrt{2}} \begin{bmatrix} 1 & j & 0 \\ 1 & -j & 0 \\ 0 & 0 & \sqrt{2} \end{bmatrix} \tag{29}$$

$$Y_{FLdq0} = \frac{H_{id} H_{del} H_{dc} (H_{PLL}^i (H_{dec} - H_{ci}))}{I - H_{FLid} H_{del} H_{dc} (H_{dec} - H_{ci})} + \frac{H_{FLid} H_{del} (H_{PLL}^d + (H_{FLid} H_{del})^{-1} Z_{FLout}^{-1})}{I - H_{FLid} H_{del} H_{dc} (H_{dec} - H_{ci})} \tag{30}$$

where

$$Z_{FLout} = \begin{bmatrix} sL_f + R_f & \omega L_f & 0 \\ -\omega L_f & sL_f + R_f & 0 \\ 0 & 0 & s(L_f + 3L_n) + R_f + 3R_n \end{bmatrix} \tag{31}$$

$$H_{FLid} = \begin{bmatrix} \frac{-(sL_f + R_f)U_{dc}}{(sL_f + R_f)^2 + (\omega L_f)^2} & \frac{\omega L_f U_{dc}}{(sL_f + R_f)^2 + (\omega L_f)^2} & 0 \\ -\frac{\omega L_f U_{dc}}{(sL_f + R_f)^2 + (\omega L_f)^2} & \frac{-(sL_f + R_f)U_{dc}}{(sL_f + R_f)^2 + (\omega L_f)^2} & 0 \\ 0 & 0 & \frac{-U_{dc}}{s(3L_n + L_f) + 3R_n + R_f} \end{bmatrix} \tag{32}$$

It should be noted that the main contribution of paper [27] is to establish the impedance model of the three-phase four-leg inverter and verify the decoupling relationships between the zero-sequence component and the positive-sequence component as well as the negative-sequence component. Compared to paper [27], although the derivation process in this paper for positive-sequence impedance and negative-sequence impedance is similar, the derivation process for zero-sequence impedance is completely different due to the different zero-sequence path and zero-sequence current control strategy.

The MATLAB/Simulink simulation is implemented for the purpose of verifying the correctness of the established impedance model. The frequency scanning result and the established impedance model of TFSCI and TFGI are presented in Figure A1 in Appendix B. In Figure A1,  $Y_{ij}$  denotes the  $i$ th element in the  $j$ th column in the admittance matrix of TFSCI  $Y_{SCpn0}$  and the admittance matrix of TFGI  $Y_{FLpn0}$ . From Figure A1, the established impedance model matches the measurement result well, which indicates that the established impedance model is accurate.



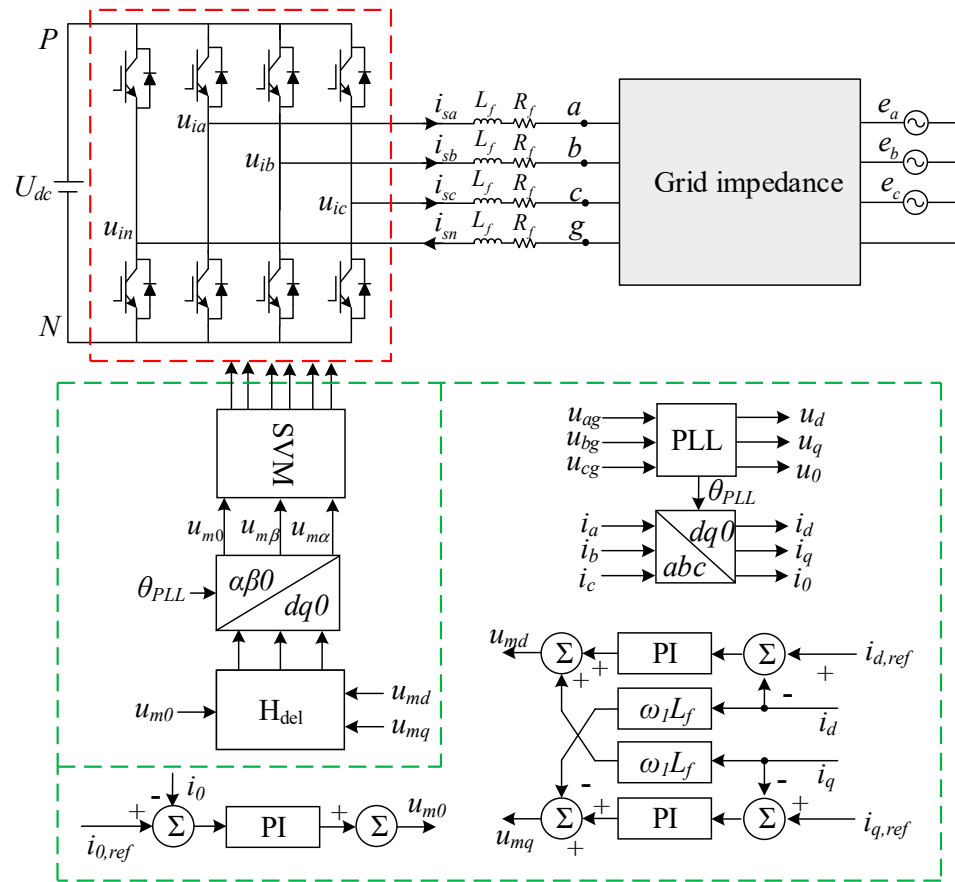


Figure 6. Block diagram of TFGI.

### 3. Comparison of Impedance Characteristics between TFSCI and TFGI

According to Equations (26) and (28), the negative-sequence impedance and positive-sequence impedance of TFGI and TFSCI are the same, and are also similar to those of the three-phase three-wire inverter [21–25]. To avoid a repetitive discussion of similar content, a detailed analysis of the negative-sequence impedance and the positive-sequence impedance will not be presented in this article. In the three-phase four-wire inverter, the zero-sequence impedance is special compared to the three-phase three-wire inverter. Hence, the zero-sequence impedance characteristics of TFSCI and TFGI will be analyzed in this section.

#### 3.1. Zero-Sequence Impedance Characteristics of TFSCI

From (24), the zero-sequence admittance can be obtained as,

$$Y_{z\_TFSCI} = \frac{1}{K_m * (k_{0ip} + k_{0ii}/s + \frac{3}{2sC_{dc}}(k_{0vp} + k_{0vi}/s)) + s(3L_n + L_f) + 3R_n + R_f} \quad (33)$$

By organizing the above equation, the following equation can be obtained,

$$Y_{z\_TFSCI} = \frac{1}{K_m * \left( R_{z\_TFSCI} + sL_{z\_TFSCI} + \frac{1}{s(C_{z\_TFSCI})} \right)} \quad (34)$$

where

$$\begin{aligned} R_{z\_TFSCI} &= k_{0ip} + \frac{3k_{0vi}}{2C_{dc}s^2} + 3R_n + R_f \\ L_{z\_TFSCI} &= 3L_n + L_f \\ C_{z\_TFSCI} &= \frac{2C_{dc}}{3k_{0vp} + 2C_{dc}k_{0ii}} \end{aligned}$$

From (32), it shows that the zero-sequence admittance of TFSCI is relevant not only to the filter parameters and zero-sequence current controller parameters, but the DC voltage balance PI controller parameters and the DC-side capacitor as well. According to Equation (32), zero-sequence admittance will reach an amplitude peak when  $|sL_{z\_TFSCI}| = 1/|sC_{z\_TFSCI}|$ , and the value of the amplitude peak is decided by  $R_{z\_TFSCI}$  according to Equation (32). An evident fact can be achieved that a larger  $R_{z\_TFSCI}$  will bring a lower amplitude peak.

Figure 7 shows bode diagrams of TFSCI when different filter parameters are applied. As the filter inductance  $L_f$  and  $L_n$  increase, the amplitude peaks occur at lower frequencies. Under the same filter inductance, the zero-sequence admittance gradually transitions from inductive characteristics to capacitive characteristics as the frequency increases.

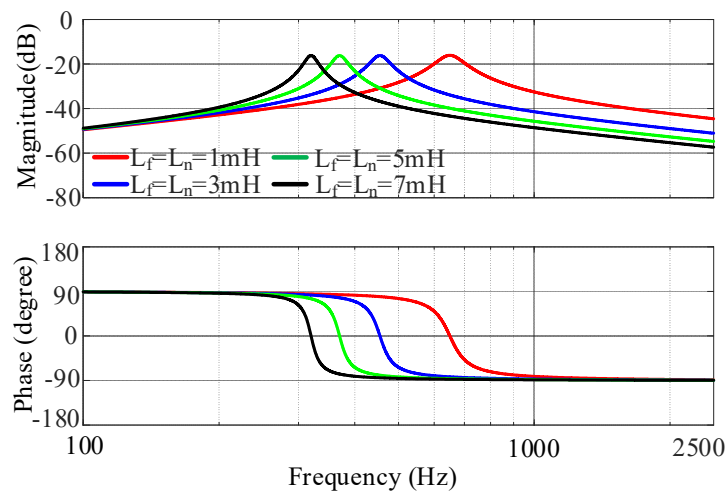


Figure 7. The zero\_sequence admittance bode diagrams of TFSCI under different filter parameters.

Figure 8 shows the zero-sequence admittance bode diagrams of TFSCI under different control bandwidths of the zero-sequence current controller. Under the same control bandwidth, the zero-sequence admittance gradually transitions from inductive characteristics to capacitive characteristics as the frequency increases. As the control bandwidth increases, the amplitude peak occurs at higher frequencies with lower amplitude due to a larger  $R_{z\_TFSCI}$  and smaller  $C_{z\_TFSCI}$ .

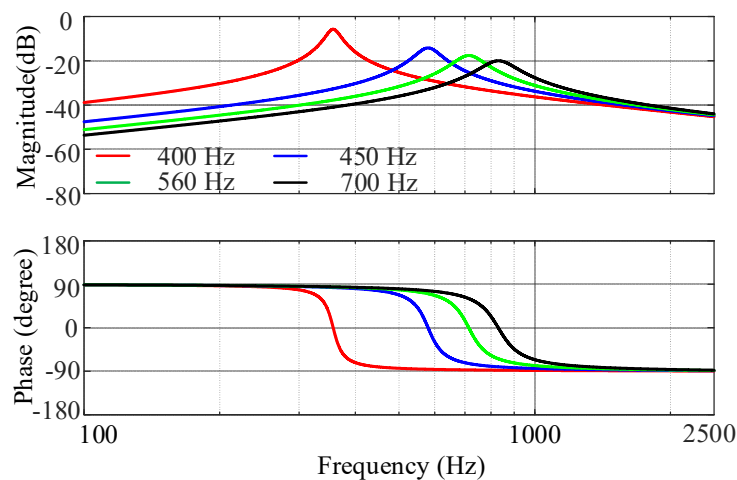
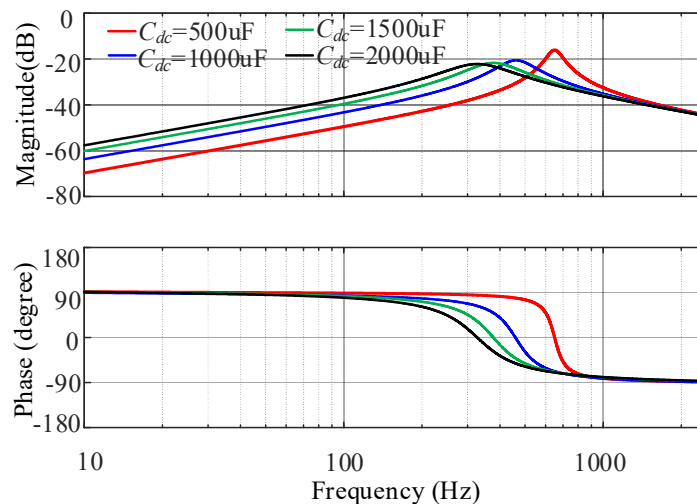


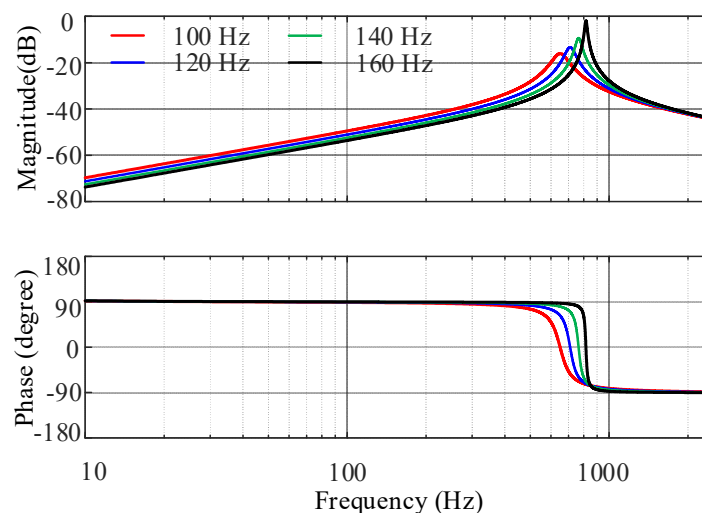
Figure 8. The zero\_sequence admittance bode diagrams of TFSCI under different control bandwidths of zero-axis current controller.

Figure 9 shows bode diagrams of the zero-sequence admittance of TFSCI when different DC-side capacitor  $C_{dc}$  values are applied. As the capacitor increases, the amplitude peak occurs at a lower frequency with lower amplitude. The reason is that the  $C_{z\_TFSCI}$  and  $R_{z\_TFSCI}$  will increase as  $C_{dc}$  increases. The larger  $C_{z\_TFSCI}$  will lead the amplitude peak to occur at a lower frequency, and the larger  $R_{z\_TFSCI}$  brings a lower amplitude peak and a wider transition zone from inductive characteristics to capacitive characteristics.



**Figure 9.** The zero\_sequence admittance bode diagrams of TFSCI under different DC\_side capacitors  $C_{dc}$ .

Figure 10 shows bode diagrams of the zero-sequence admittance of TFSCI under different voltage loop bandwidth used in the zero-axis DC voltage loop. It can be seen that the zero-sequence admittance gradually transitions from inductive characteristics to capacitive characteristics as the frequency increases. As the capacitor increases, the amplitude peak occurs at higher frequencies with higher amplitude. This is because the  $C_{z\_TFSCI}$  and  $R_{z\_TFSCI}$  will decrease as the control bandwidth increases. The smaller  $C_{z\_TFSCI}$  will lead the amplitude peak to occur at a higher frequency and the smaller  $R_{z\_TFSCI}$  brings a higher amplitude peak and a narrower transition zone from inductive characteristics to capacitive characteristics.



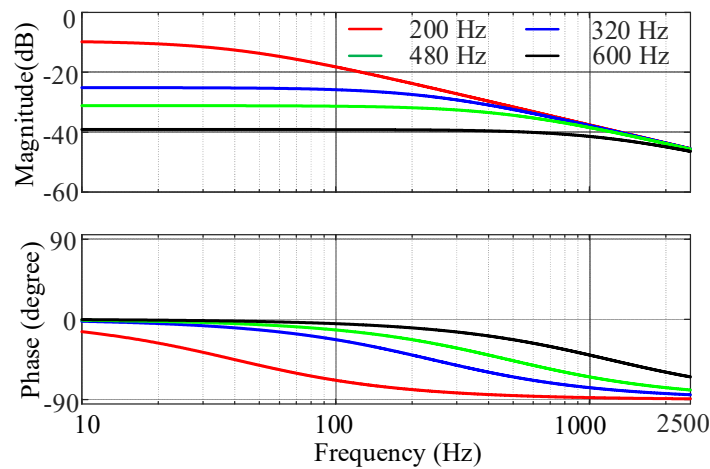
**Figure 10.** The zero\_sequence admittance bode diagrams of TFSCI under different bandwidths of DC\_voltage balance PI controller.

### 3.2. Zero-Sequence Impedance Characteristics of TFGI

From Equation (26), the zero-sequence admittance of TFGI can be expressed as,

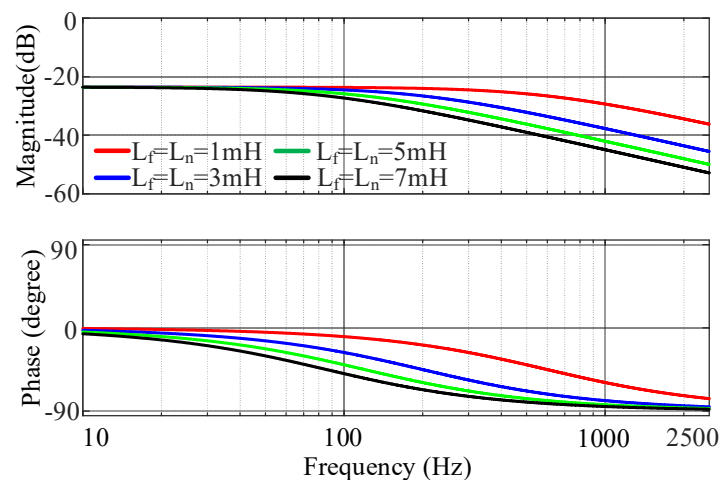
$$Y_{z\_TFGI} = 1 / \left( s(3L_n + L_f) + 3R_n + R_f + \left( k_{0ip} + \frac{k_{0ii}}{s} \right) \right) \quad (35)$$

Figure 11 shows zero-sequence admittance bode diagrams of TFGI under different control bandwidths of the zero-axis current controller. Figure 11 shows that as the control bandwidth increases, the region with resistive characteristics gradually expands, and the admittance magnitude becomes smaller. Under the same bandwidth parameters, the zero-sequence admittance gradually changes from resistive characteristics to capacitive characteristics with the frequency increasing.



**Figure 11.** The zero\_sequence admittance bode diagrams of TFSCI under different control bandwidths of zero\_axis current controller.

Figure 12 shows the zero-sequence admittance bode diagrams of TFGI when different filter parameters are applied. From Figure 12, the amplitude of the zero-sequence admittance of TFGI decreases and the region with resistive characteristic shrinks as the AC-side filter increases. Additionally, the zero-sequence admittance gradually transitions from resistive characteristics to capacitive characteristics as the frequency increases.



**Figure 12.** The zero\_sequence admittance bode diagrams of TFGI under different filter parameters.

### 4. Stability Analysis

Based on the impedance stability theory [25], the small-signal stability of the three-phase four-wire grid-connected inverter system will be analyzed in this section. In order to investigate different impedance conditions of the distribution network and microgrid, the grid-side impedance can be intuitively equivalent to the circuit in Figure 13. In Figure 13, the capacitor  $C_g$  represents the parallel compensation degree, and the inductor  $L_g$  represents the strength of the grid.  $R_{Cg}$  and  $R_{Lg}$  present the parasitic resistance [10–12]. Hence, the grid impedance matrix can be expressed as,

$$\mathbf{Z}_g = \begin{bmatrix} Z_{gp} & 0 & 0 \\ 0 & Z_{gn} & 0 \\ 0 & 0 & Z_{g0} \end{bmatrix} = \begin{bmatrix} \mathbf{Z}_{gpn} & 0 \\ 0 & \mathbf{Z}_{g0} \end{bmatrix} \tag{36}$$

where

$$Z_{gp} = Z_{gn} = \frac{(sL_g + R_{Lg})(sC_g R_{Cg} + 1)}{R_{Cg}(sL_g + R_{Lg}) + sC_g R_{Cg} + 1} \tag{37}$$

$$Z_{g0} = \frac{(1 + sC_g R_{Cg})(s(L_g + 3L_{gn}) + R_{Lg} + 3R_{Lgn})}{sC_g(s(L_g + 3L_{gn}) + R_{Lg} + 3R_{Lgn}) + 1 + sC_g R_{Cg}}$$

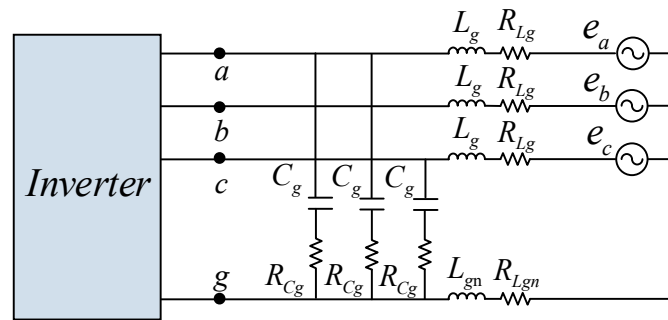


Figure 13. The equivalent circuit of the grid impedance.

To analyze the system stability, the generalized Nyquist criterion is applied to the Nyquist plot of the eigenvalues of  $\mathbf{Y}_{ipn0} * \mathbf{Z}_g$ , where the impedance ratio matrix can be written as,

$$\mathbf{L} = \mathbf{Y}_{ipn0} * \mathbf{Z}_g = \begin{bmatrix} \mathbf{Y}_{ipn} \mathbf{Z}_{gpn} & 0 \\ 0 & \mathbf{Y}_{i0} \mathbf{Z}_{g0} \end{bmatrix} \tag{38}$$

From Equation (37), since the relationship between zero-sequence impedance and negative-sequence impedance as well as positive impedance is decoupled, the premise for the system to remain stable is that the positive and negative subsystems and the zero-sequence subsystem can remain stable at the same time. In other words, the system instability may be caused by positive- and negative-sequence components or may be brought about by the zero-sequence component.

Based on the above stability analysis theory, the adaptability and instability risk of TFSCI and TFGI in two typical grids, weak grids with and without parallel compensation, are studied in this section.

#### 4.1. Weak Grid without Parallel Compensation

When the power grid is a weak grid without parallel compensation, the impedance of the grid can be expressed as shown in Equation (38). According to reference [26,27], the three-phase three-wire grid-connected inverter system has the instability risk caused by the SRF-PLL in the weak grid. Since the SRF-PLL also exists in the TFGI and TFSCI, along with the decoupled relationship between zero-sequence impedance and positive-sequence impedance as well as negative-sequence impedance, the three-phase four-wire inverter

also has the instability risk caused by SRF-PLL. To avoid a repetitive discussion of similar content, a detailed analysis is not given in this paper. The figure below shows the root locus of  $Y_{ipn}Z_{gpn}$  when the proportional gain of SRF-PLL changes from 0.58 to 2.85. According to Figure 14, there is a risk of instability at 265 Hz.

$$Z_g = \begin{bmatrix} Z_{gp} & 0 & 0 \\ 0 & Z_{gn} & 0 \\ 0 & 0 & Z_{g0} \end{bmatrix} = \begin{bmatrix} Z_{gpn} & 0 \\ 0 & Z_{g0} \end{bmatrix} \tag{39}$$

where

$$Z_{gpn} = \begin{bmatrix} sL_g + R_{Lg} & 0 \\ 0 & sL_g + R_{Lg} \end{bmatrix}$$

$$Z_{g0} = s(L_g + 3L_{gn}) + R_{Lg} + 3R_{Lgn}$$

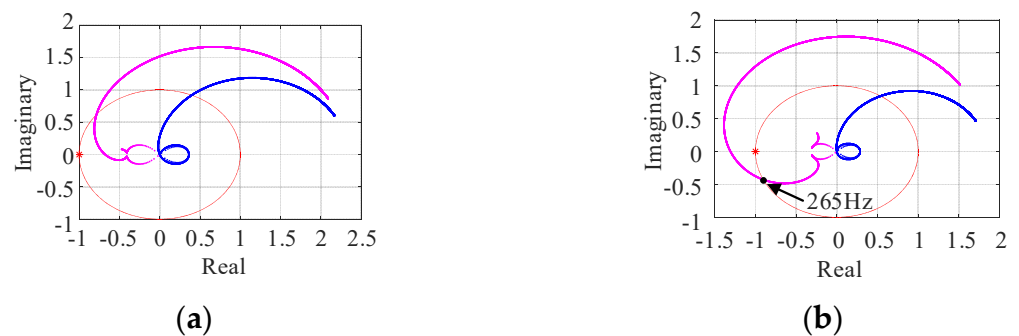


**Figure 14.** Characteristic root locus of  $Y_{ipn} \cdot Z_{gpn}$ . (a) Proportional gain of SRF-PLL  $k_{pp} = 0.58$ . (b) Proportional gain of SRF-PLL  $k_{pp} = 2.85$ .

Figure 15 shows the root locus of the inverter current when the phase currents  $i_a, i_b,$  and  $i_c$  change from 0.5 p.u. to 1 p.u. According to Figure 14a, there is no risk of instability when  $i_a = i_b = i_c = 0.5$  p.u. According to Figure 14b, it also can be seen that there is a risk of instability at 265 Hz when  $i_a = i_b = i_c = 1$  p.u.

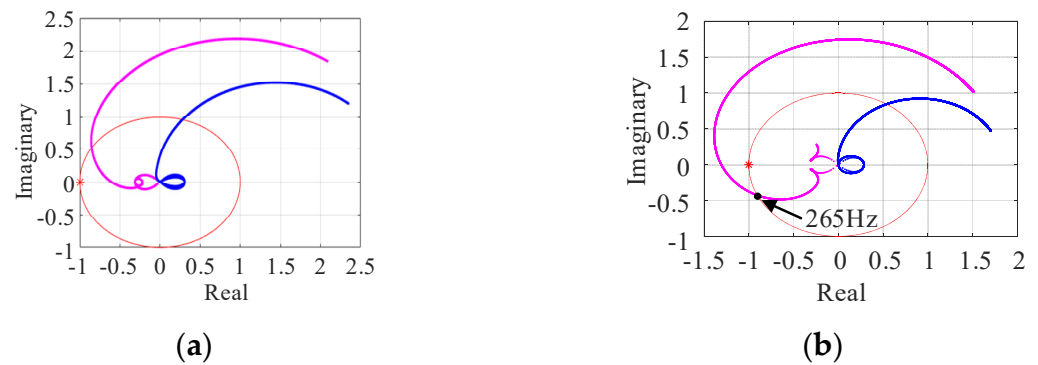


**Figure 15.** Characteristic root locus of  $Y_{ipn} \cdot Z_{gpn}$ . (a) Proportional gain of SRF-PLL  $k_{pp} = 2.85$  and phase current  $i_a = i_b = i_c = 0.5$  p.u. (b) Proportional gain of SRF-PLL  $k_{pp} = 2.85$  and phase currents  $i_a = i_b = i_c = 1$  p.u.

In addition, the TFSCI also has the instability risk brought by the zero-sequence subsystem because, according to the bode diagram of the TFSCI shown in Figure 7, the impedance characteristics of the TFSCI undergo a gradual transition from capacitive characteristics to inductive characteristics. According to stability theory of impedance proposed in reference [25], in the frequency region where the zero-sequence impedance shows capacitive characteristics, if the phase angle difference of impedance between TFSCI and the weak grid at the impedance amplitude intersection is close to  $180^\circ$ , it will cause system small-signal

instability. Figure 16 shows the zero-sequence admittance bode diagrams of TFSCI and grid when the risk of small-signal instability is caused by the zero-sequence component. In Figure 15,  $Y_{SC33}$  is the zero-sequence admittance of the TFSCI and  $Y_{g0}$  is the zero-sequence admittances of grid.

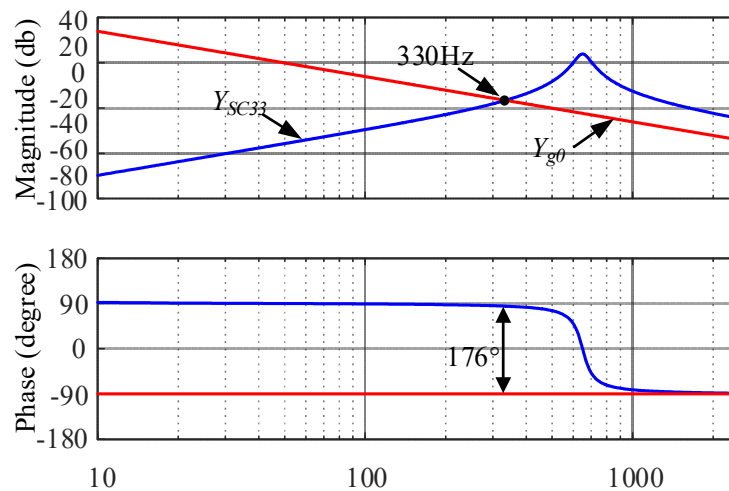


**Figure 16.** The zero\_sequence admittance bode diagrams of TFSCI and grid when the small\_signal instability is caused by the zero\_sequence component.

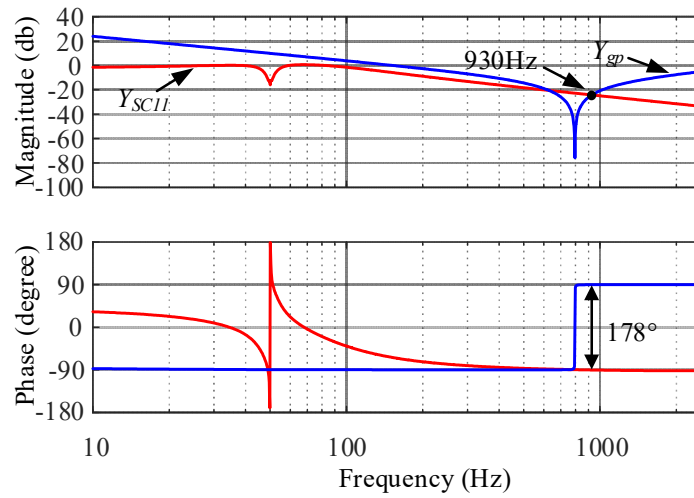
According to the above analyses, the difference in zero-sequence impedance will lead to poor adaptability and a higher risk of instability of TFSCI compared with TFGI in the weak grid.

#### 4.2. Weak Grid with Parallel Compensation

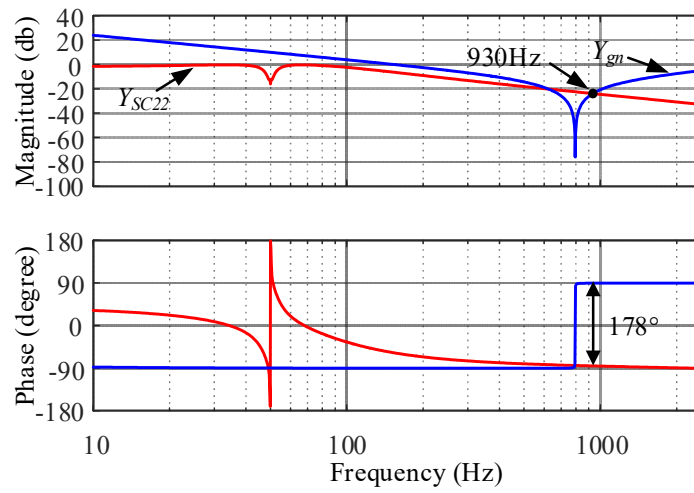
Under the weak grid with parallel compensation, the grid impedance can be expressed as Equation (34).

Combined with the bode diagram of the split capacitor inverter impedance, we know that there is a risk of high-frequency resonance in the system under the parallel compensation grid. The bode diagram of the capacitor split inverter impedance and grid impedance are shown in Figure 17. It can be seen from Figure 17 that the positive-sequence and negative-sequence impedances of the inverter are inductive at high frequency and the phase difference between the impedance of the TFSCI system and the impedance of the grid is  $178^\circ$ , close to  $180^\circ$ , at the amplitude intersection point 930 Hz. The zero-sequence impedance characteristics of the inverter gradually transition from capacitive to inductive and the phase difference between the impedance of TFSCI system and the impedance of the grid is  $176^\circ$ , close to  $180^\circ$ , at the amplitude intersection point 356 Hz. Figure 16 reveals that the system has a risk of resonance at 356 Hz and 930 Hz.

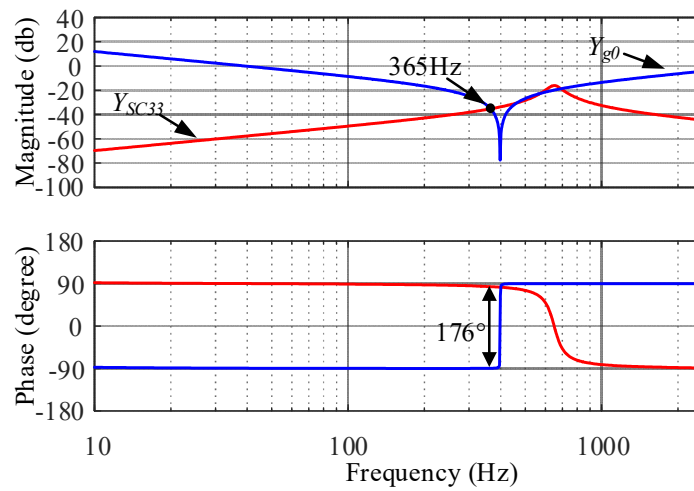
Similarly, combined with the bode diagram of the TFGI impedance, there is a risk of high-frequency resonance in the system. The bode diagram of the TFGI admittance and grid admittance are shown in Figure 18. According to Figure 18, the zero-sequence impedance, negative-sequence impedance, and positive-sequence impedance of TFGI are inductive at high frequency, and the phase difference between the impedance of TFSCI system and the impedance of grid is close to  $180^\circ$  at the amplitude intersection points 930 Hz and 460 Hz. Figure 18 reveals that the system has a risk of resonance at 930 Hz and 460 Hz.



(a) Positive-sequence admittance



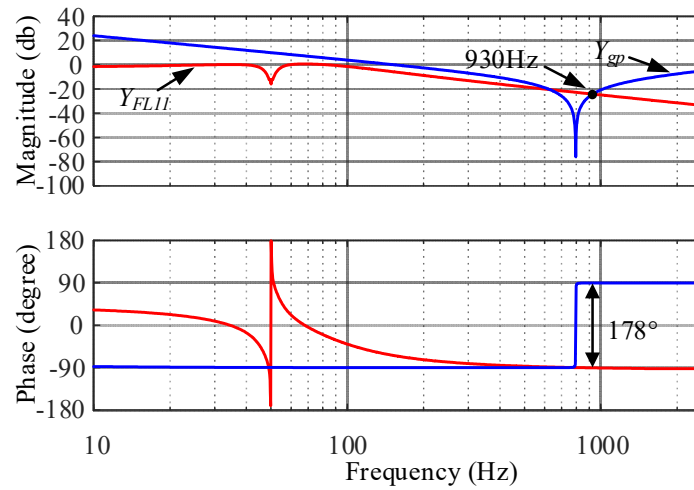
(b) Negative-sequence admittance



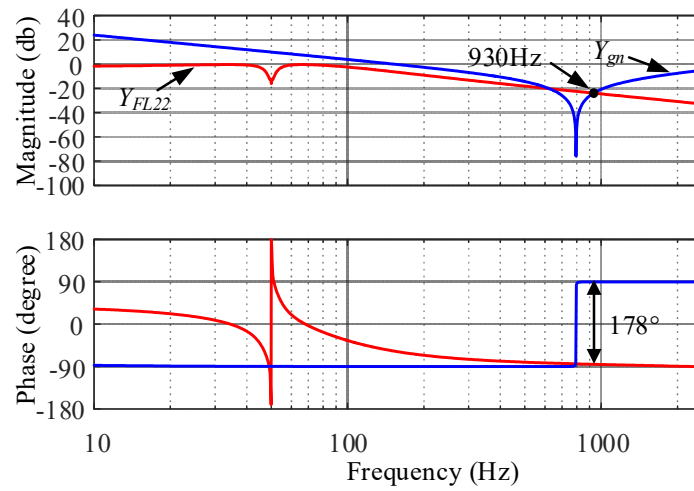
(c) Zero-sequence admittance

Figure 17. Admittance model of TFSCI and the grid, when the small\_signal instability is caused by zero-sequence component, positive\_sequence component, and negative-sequence components.

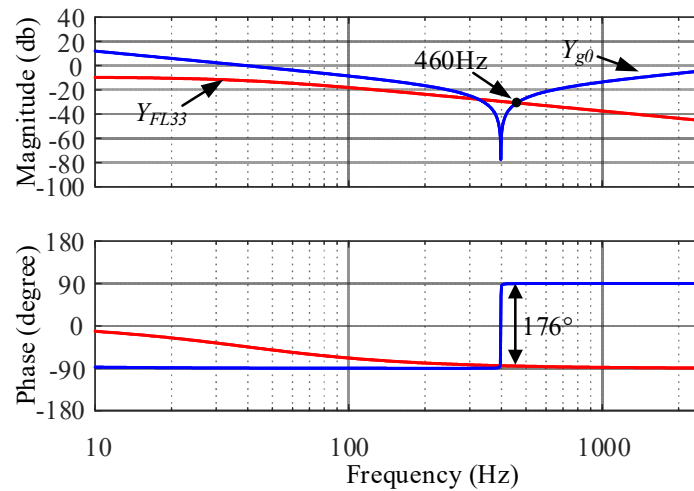




(a) Positive-sequence admittance



(b) Negative-sequence admittance



(c) Zero-sequence admittance

**Figure 18.** Admittance model of TFGI and the grid, when the small-signal instability is caused by zero-sequence, positive-sequence, and negative-sequence components.

## 5. Experimental Verification

To better verify the achieved conclusions, the hardware platform based on control-hardware-in-loop (CHIL) is established, which can be seen in Figure 19. The models of the three-phase four-wire split capacitor grid-connected inverter system and the three-phase four-leg grid-connected inverter system are established in Typhoon 602+. The controllers of TFSCI and TFGI are carried out on a TMS320F28335/Spartan6 XC6SLX16 DSP + FPGA control board. The CHIL was used to analyze and verify the conclusion presented in [28,29]. The corresponding parameters of the system are listed in Tables A1 and A2 in Appendix C.

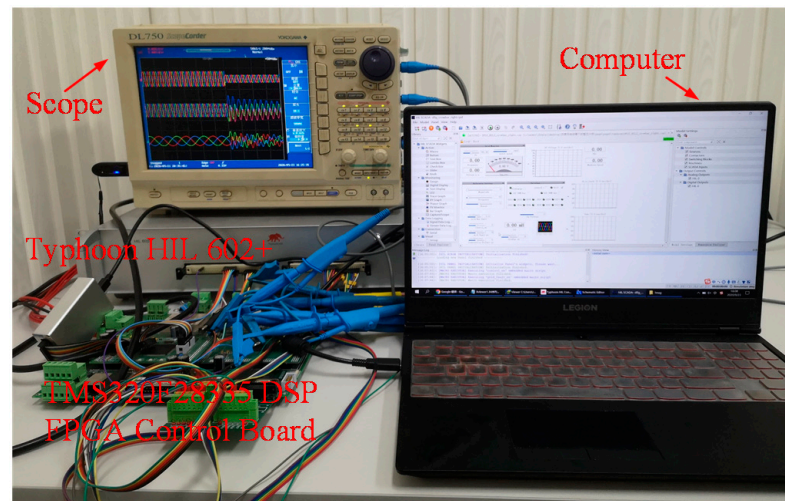


Figure 19. Hardware platform of CHIL experiment.

Figure 20 shows the voltages, currents, active power, and reactive power of the TFSCI when the SRF-PLL proportional gain ( $k_{pp}$ ) changes from 0.58 to 2.85. Figure 21 shows the FFT analysis of phase-a current ( $i_a$ ) when  $k_{pp} = 2.85$ . It can be seen from Figures 20 and 21 that there are considerable harmonic components at 174 Hz and 274 Hz in the system. From Figure 21, it also can be found that instability of the positive–negative-sequence sub-system occurs due to there being no zero-sequence harmonics in the system. The instability characteristics coincide with Figure 14.

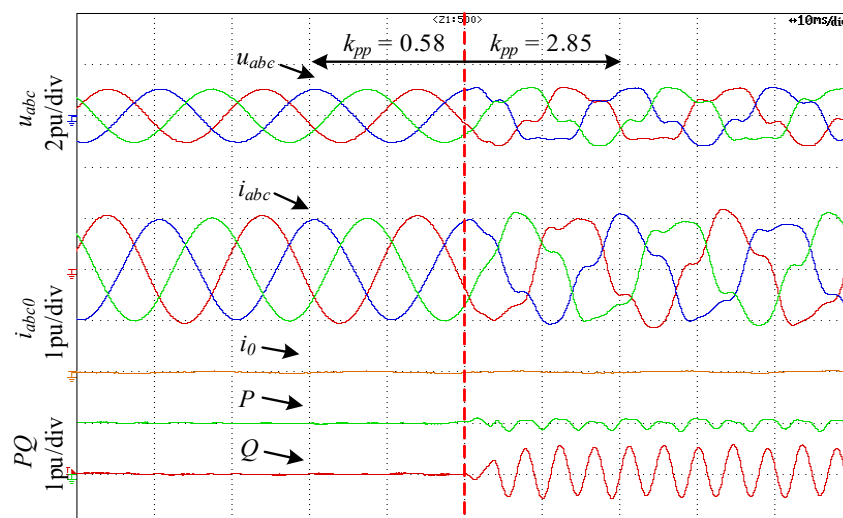


Figure 20. Experiment results of the instability of positive–negative-sequence sub-system when  $k_{pp}$  changes from 0.58 to 2.85.

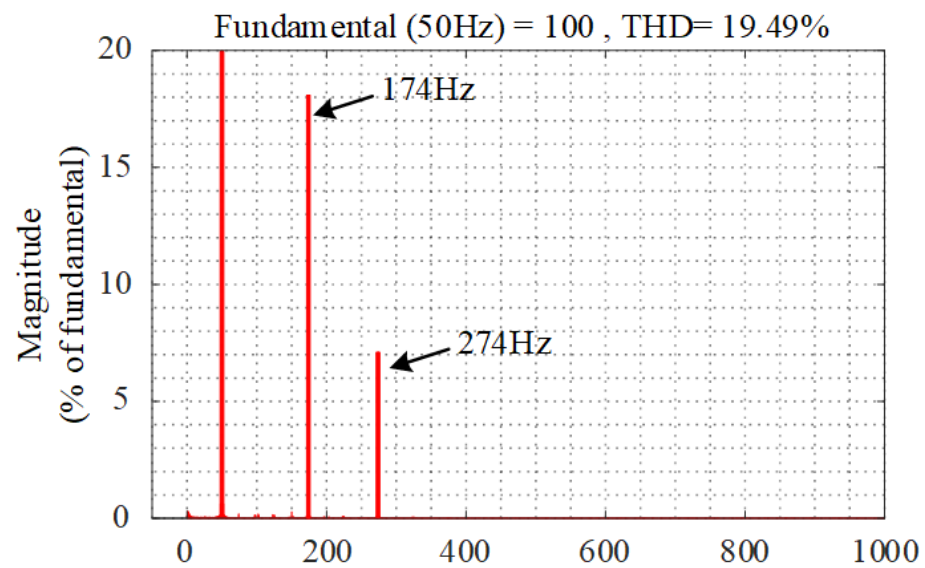


Figure 21. FFT analysis of  $i_a$  when  $k_{pp} = 2.85$ .

Figure 22 shows the voltages, currents, active power, and reactive power of the TFSCI when the SRF-PLL proportional gain  $k_{pp} = 2.85$  and phase currents  $i_a$ ,  $i_b$ , and  $i_c$  change from 0.5 p.u. to 1 p.u. Figure 23 shows the FFT analysis of phase-a current ( $i_a$ ) when  $i_a = i_b = i_c = 1$  p.u. It can be seen from Figures 22 and 23 that there are considerable harmonic components at 174 Hz and 274 Hz in the system. From Figure 22, it can also be found that instability of the positive- and negative-sequence sub-system occurs due to there being no zero-sequence harmonics in the system. The instability characteristics coincide with Figure 15.

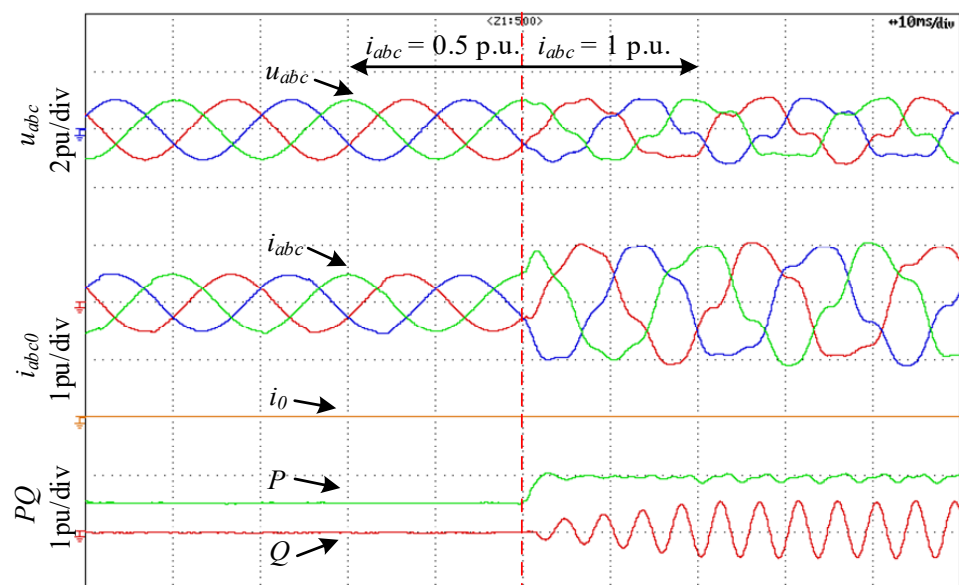


Figure 22. Experiment results of the instability of positive–negative-sequence sub-system when  $k_{pp}$  changes from 0.58 to 2.85.

Figure 24 shows the voltages, currents, active power, and reactive power of the TFSCI when the proportional gain of current PI controller ( $k_{0ip}$ ) changes from 3 to 10. Figure 25 shows the FFT analysis of phase-a current ( $i_a$ ) when  $k_{0ip} = 10$ . It can be seen from Figures 24 and 25 that there is a considerable harmonic component at 327 Hz in the system. From Figure 24, it also can be seen that instability of zero-sequence sub-system occurs. The instability characteristics coincide with Figure 16.

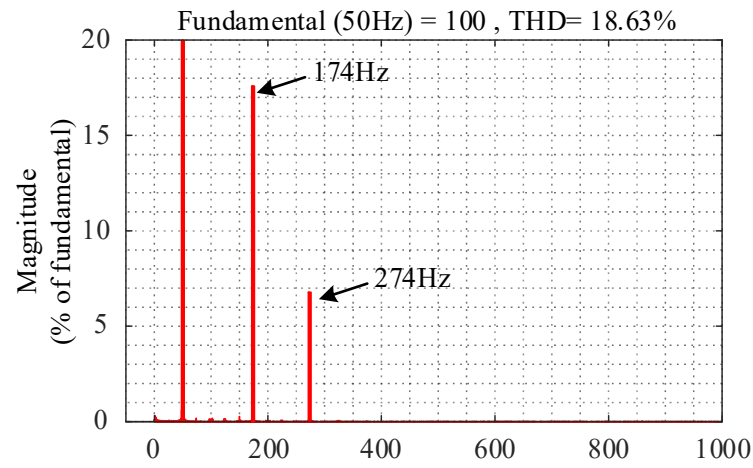


Figure 23. FFT analysis of  $i_a$  when  $i_a = i_b = i_c = 1$  p.u.

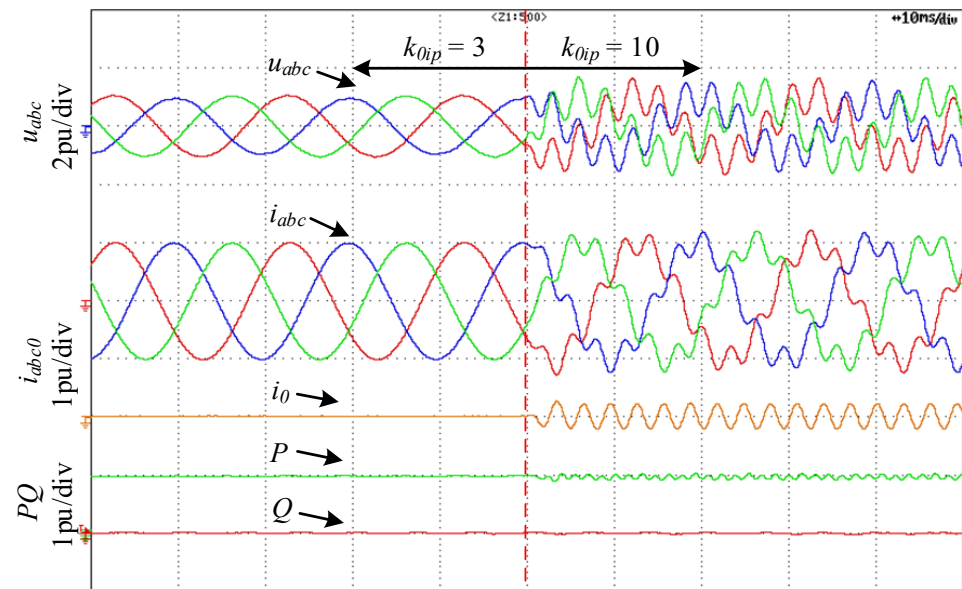


Figure 24. Experiment results of the instability of zero-sequence sub-system when  $k_{0ip}$  changes from 3 to 10.

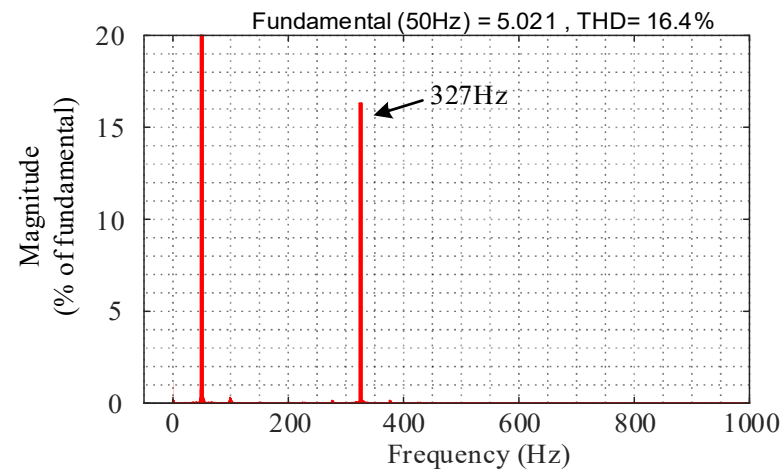


Figure 25. FFT analysis of  $i_a$  when  $k_{0ip} = 10$ .

Figure 26 shows the voltages, currents, active power, and reactive power of the TFSCI connected to the parallel compensation grid when capacitor  $C_g$  changes from 0 to 40  $\mu\text{F}$ . Figure 27 shows the FFT analysis of  $i_a$  when  $C_g = 40 \mu\text{F}$ . It can be seen from Figures 26 and 27 that there are considerable harmonic components at 365 Hz and 930 Hz in the system. From Figure 26, it also can be found that the resonance at 431 Hz is caused by the zero-sequence components and the resonance at 930 Hz is caused by the negative-sequence component and the positive-sequence component. The instability characteristics coincide with Figure 17.

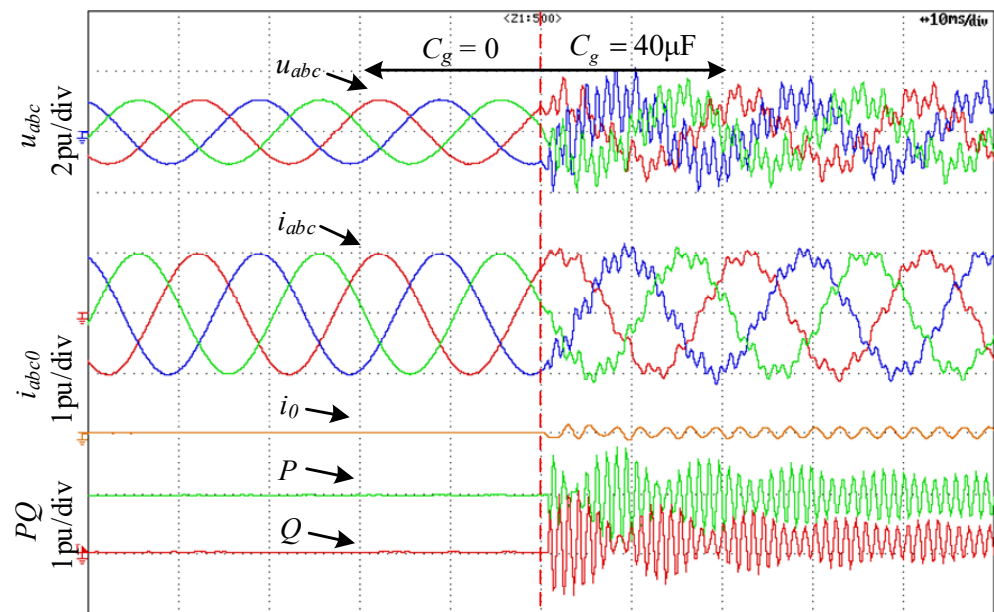


Figure 26. Experiment results of the instability of TFSCI when  $C_g$  changes from 0 to 40  $\mu\text{F}$ .

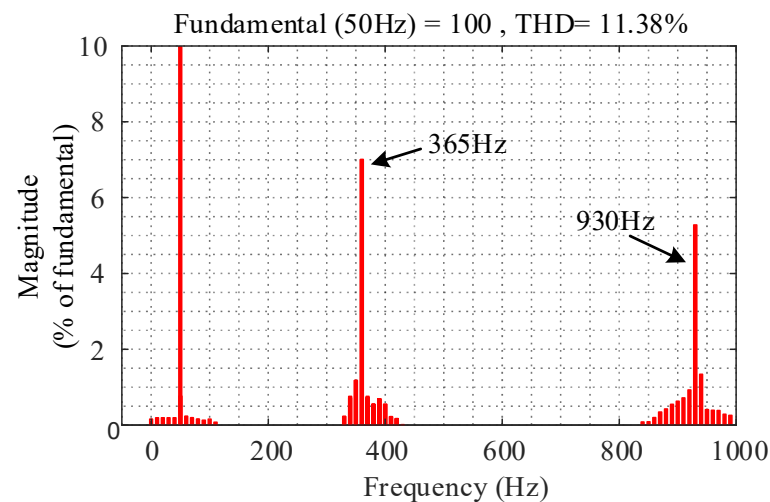


Figure 27. FFT analysis of  $i_a$  of TFSCI when  $C_g = 40 \mu\text{F}$ .

Figure 28 shows the voltages, currents, active power, and reactive power of the TFGI connected to parallel compensation grid when capacitor  $C_g$  changes from 0 to 40  $\mu\text{F}$ . Figure 29 shows the FFT analysis of phase-a current ( $i_a$ ) when  $C_g = 40 \mu\text{F}$ . It can be seen from Figures 28 and 29 that there are considerable harmonic components at 460 Hz and 930 Hz in the system. From Figure 28, it also can be seen that the resonance at 431 Hz is generated by the zero-sequence component and the resonance at 930 Hz is brought about by the positive-sequence and negative-sequence components. The instability characteristics coincide with Figure 18.

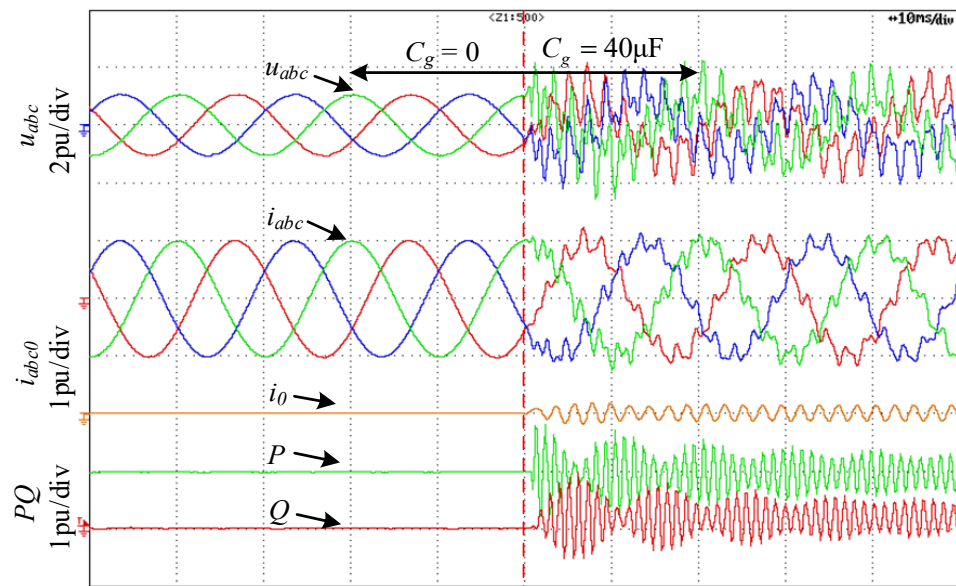


Figure 28. Experiment result of the instability of TFGI when  $C_g$  changes from 0 to 40  $\mu\text{F}$ .

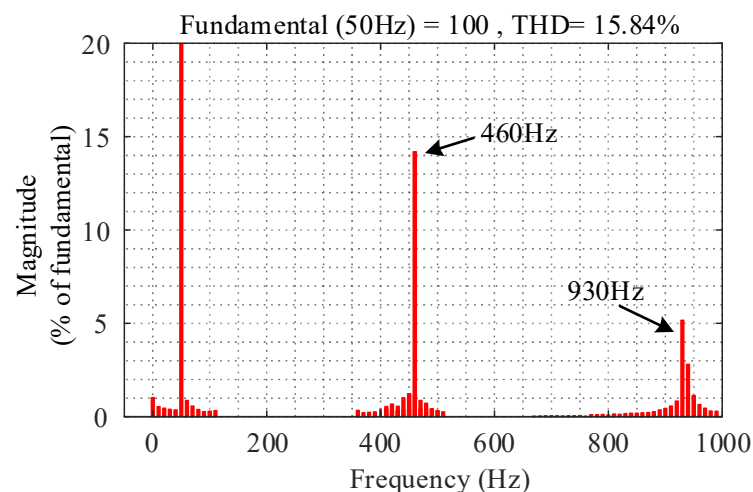


Figure 29. FFT analysis of  $i_{af}$  of TFGI when  $C_g = 40 \mu\text{F}$ .

## 6. Conclusions

The impedances of TFSCI and TFGI with consideration of the zero-sequence component were studied in this paper. The specific conclusions achieved here are as follows.

- (1) The impedance models of TFSCI and TFGI, commonly used in three-phase four-wire systems, including positive-sequence impedance, negative-sequence impedance, and zero-sequence impedance were established.
- (2) The similarity and difference of TFSCI impedance and TFGI impedance were revealed. The similarity lies in the similarity of the positive-sequence impedance and negative-sequence impedance. The difference is that the zero-sequence impedances are different, and these differences are mainly caused by the different zero-sequence current paths. The zero-sequence impedance of TFSCI has both capacitive and inductive characteristics, while the zero-sequence impedance of TFGI is mainly resistive and inductive.
- (3) The stability analysis was carried out through the impedance model, and the instability risk of the power grid under the weak grid and the parallel compensation grid were revealed. The difference in zero-sequence impedance leads to poor adaptability and higher instability risk of TFSCI compared with TFGI in the weak grid.

In addition, based on the established impedance of TFSCI and TFGI, the instability risk of the system can be analyzed through the impedance stability theory, and the phase margin can be improved when designing the system parameters to avoid system instability. When a small signal instability occurs in the system, the inverter impedance can be reshaped by changing the system parameters or the control strategy to restore the stability of the system.

**Author Contributions:** Conceptualization, Z.Y.; Investigation, Z.W.; Project administration, Y.X.; Validation, L.H.; Writing—original draft, G.F. All authors have read and agreed to the published version of the manuscript.

**Funding:** This research was funded by [the National Natural Science Fundamentation of China] grant number [51507183, 51877212, 51807197].

**Informed Consent Statement:** This research article describing a study doesn't involving humans.

**Conflicts of Interest:** The authors declare no conflict of interest.

## Appendix A

According to Figure 3, the equation of the small-signal circuit model of TFSCI can be achieved as follows:

$$\begin{bmatrix} \Delta u_d^s \\ \Delta u_q^s \\ \Delta u_0^s \end{bmatrix} = \begin{bmatrix} L_f & 0 & 0 \\ 0 & L_f & 0 \\ 0 & 0 & L_f + 3L_n \end{bmatrix} \begin{bmatrix} p\Delta i_d^s \\ p\Delta i_q^s \\ p\Delta i_0^s \end{bmatrix} + \begin{bmatrix} R_f & 0 & 0 \\ 0 & R_f & 0 \\ 0 & 0 & R_f + 3R_n \end{bmatrix} \begin{bmatrix} \Delta i_d^s \\ \Delta i_q^s \\ \Delta i_0^s \end{bmatrix} + \begin{bmatrix} \Delta d_d^s U_{dc} \\ \Delta d_q^s U_{dc} \\ \Delta u_{dc2} U_{dc} \end{bmatrix} + \begin{bmatrix} D_d^s \Delta u_{dc} \\ \Delta D_q^s \Delta u_{dc} \\ \Delta D_0^s \Delta u_{dc} \end{bmatrix} \quad (A1)$$

In this paper, the DC voltage of the inverter is assumed to be constant to simplify the modeling process.  $\Delta u_{dc} = 0$ .

Then,

$$\begin{bmatrix} \Delta u_d^s \\ \Delta u_q^s \\ \Delta u_0^s \end{bmatrix} = \begin{bmatrix} L_f & 0 & 0 \\ 0 & L_f & 0 \\ 0 & 0 & L_f + 3L_n \end{bmatrix} \begin{bmatrix} p\Delta i_d^s \\ p\Delta i_q^s \\ p\Delta i_0^s \end{bmatrix} + \begin{bmatrix} R_f & 0 & 0 \\ 0 & R_f & 0 \\ 0 & 0 & R_f + 3R_n \end{bmatrix} \begin{bmatrix} \Delta i_d^s \\ \Delta i_q^s \\ \Delta i_0^s \end{bmatrix} + \begin{bmatrix} \Delta d_d^s U_{dc} \\ \Delta d_q^s U_{dc} \\ -\Delta u_{dc2} + \Delta d_0^s U_{dc} \end{bmatrix} \quad (A2)$$

According to the Laplace transformation, the following equation can be achieved:

$$\begin{bmatrix} \Delta u_d^s \\ \Delta u_q^s \\ \Delta u_0^s \end{bmatrix} = \begin{bmatrix} sL_f + R_f & \omega L_f & 0 \\ -\omega L_f & sL_f + R_f & 0 \\ 0 & 0 & s(L_f + 3L_n) + R_f + 3R_n \end{bmatrix} \begin{bmatrix} \Delta i_d^s \\ \Delta i_q^s \\ \Delta i_0^s \end{bmatrix} + \begin{bmatrix} \Delta d_d^s U_{dc} \\ \Delta d_q^s U_{dc} \\ -\Delta u_{dc2} + \Delta d_0^s U_{dc} \end{bmatrix} \quad (A3)$$

Assuming  $\Delta d_d^s = \Delta d_q^s = \Delta d_0^s$ , the relationship between the small-signal perturbation voltage and the corresponding current in the system frame can be expressed as:

$$\begin{bmatrix} \Delta u_d^s \\ \Delta u_q^s \\ \Delta u_0^s \end{bmatrix} = \begin{bmatrix} sL_f + R_f & \omega L_f & 0 \\ -\omega L_f & sL_f + R_f & 0 \\ 0 & 0 & s(L_f + 3L_n) + R_f + 3R_n \end{bmatrix} \begin{bmatrix} \Delta i_d^s \\ \Delta i_q^s \\ \Delta i_0^s \end{bmatrix} + \begin{bmatrix} 0 \\ 0 \\ -\Delta u_{dc2} \end{bmatrix} \quad (A4)$$

Combining Equation (4), the transfer function matrix from perturbation voltage to current response in the system frame can be expressed as follows.

$$\mathbf{Z}_{SCout} = \begin{bmatrix} sL_f + R_f & \omega L_f & 0 \\ -\omega L_f & sL_f + R_f & 0 \\ 0 & 0 & s(L_f + 3L_n) + R_f + 3R_n - \frac{3}{2sC} \end{bmatrix} \quad (A5)$$

## Appendix B

Figure A1 shows the bode diagrams of the analytical admittance and frequency scanning admittance of the TFSCI and TFGI, in which  $Y_{ij}$  denotes the  $i$ th element in the  $j$ th column in the admittance matrix of TFSCI  $\mathbf{Y}_{SCpn0}$  and the admittance matrix of TFGI  $\mathbf{Y}_{FLpn0}$ .

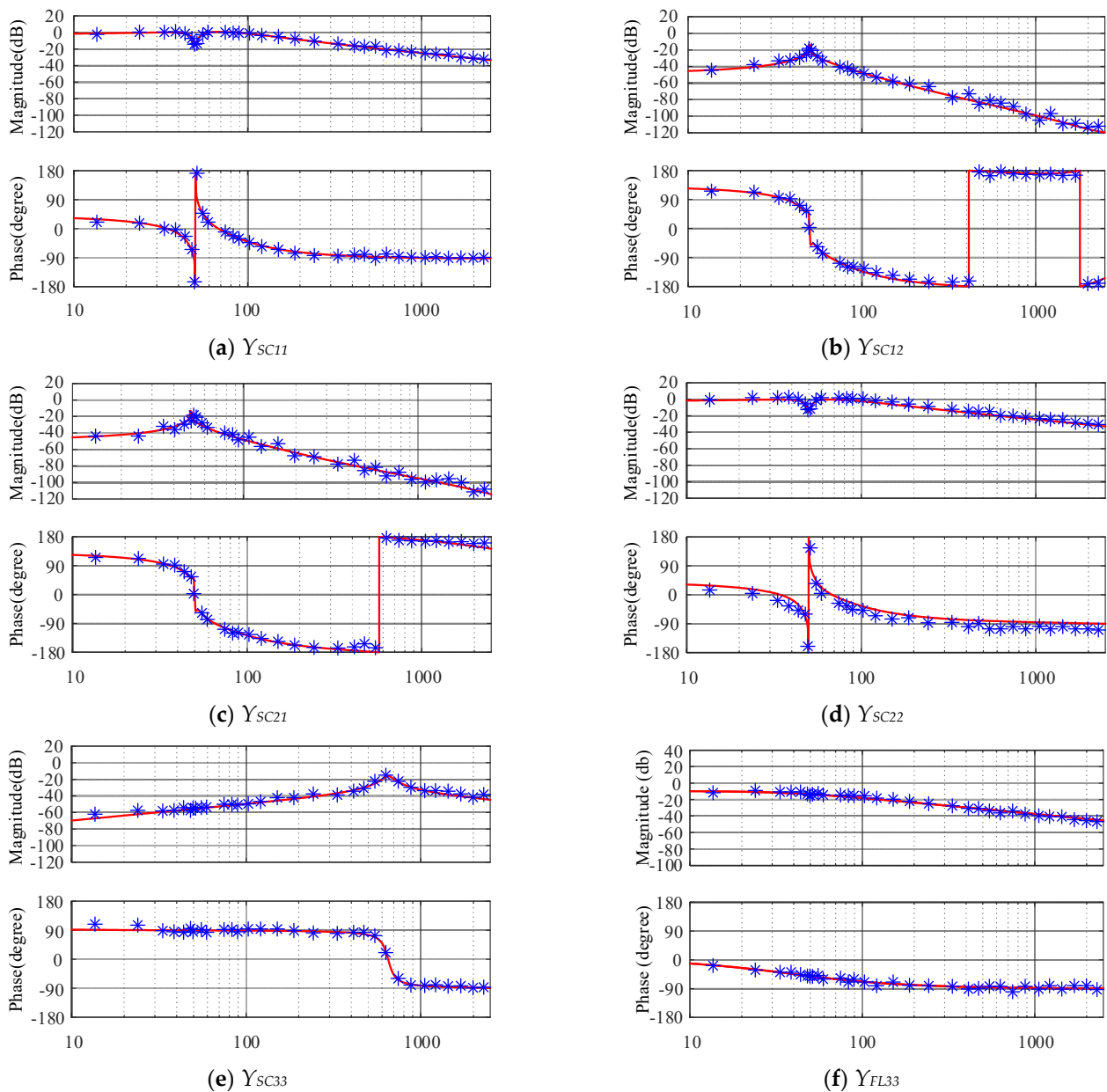


**Figure A1.** Bode diagram comparison of the output admittance of the inverter (red curve denotes the established model result and blue asterisk denotes the frequency scanning measurement result).

## Appendix C

**Table A1.** Three-phase four-wire split capacitor inverter parameters.

| Symbol    | Parameter                                      | Value         |
|-----------|--|---------------|
| $U_s$     | Rated voltage                                  | 380 V         |
| $P_n$     | Rated power                                    | 30 kW         |
| $f_1$     | Fundamental frequency                          | 50 Hz         |
| $f_s$     | Switching frequency                            | 5 kHz         |
| $L_f$     | Filter inductance                              | 3 mH          |
| $R_{L_f}$ | Parasitic resistance of filter inductance      | 0.02 $\Omega$ |
| $k_{pp}$  | SRF-PLL proportional gain                      | 0.58          |
| $k_{pi}$  | SRF-PLL integral gain                          | 0.25          |
| $k_{dip}$ | $d$ -axis current controller proportional gain | 1             |



**Table A1.** Cont.

| Symbol    | Parameter  | Value |
|-----------|--|-------|
| $k_{dii}$ | $d$ -axis current controller integral gain                 | 18    |
| $k_{qip}$ | $q$ -axis current controller proportional gain             | 1     |
| $k_{qii}$ | $q$ -axis current controller integral gain                 | 18    |
| $k_{0ip}$ | 0-axis current controller proportional gain                | 3     |
| $k_{0ii}$ | 0-axis current controller integral gain                    | 54    |
| $k_{dcp}$ | Proportional parameter of DC voltage balance PI controller | 2.1   |
| $k_{dci}$ | Integral parameter of DC voltage balance PI controller     | 4.2   |

**Table A2.** Three-phase four-leg inverter parameters.

| Symbol    | Parameter                                      | Value         |
|-----------|--|---------------|
| $U_s$     | Rated voltage                                  | 380 V         |
| $P_n$     | Rated power                                    | 30 kW         |
| $f_1$     | Fundamental frequency                          | 50 Hz         |
| $f_s$     | Switching frequency                            | 5 kHz         |
| $L_f$     | Filter inductance                              | 3 mH          |
| $R_{Lf}$  | Parasitic resistance of filter inductance      | 0.02 $\Omega$ |
| $k_{pp}$  | SRF-PLL proportional gain                      | 0.58          |
| $k_{pi}$  | SRF-PLL integral gain                          | 0.25          |
| $k_{dip}$ | $d$ -axis current controller proportional gain | 1             |
| $k_{dii}$ | $d$ -axis current controller integral gain     | 18            |
| $k_{qip}$ | $q$ -axis current controller proportional gain | 1             |
| $k_{qii}$ | $q$ -axis current controller integral gain     | 18            |
| $k_{0ip}$ | 0-axis current controller proportional gain    | 3             |
| $k_{0ii}$ | 0-axis current controller integral gain        | 54            |

**Table A3.** List of some special symbols.

| Symbol | Parameter                              |
|--------|--|
| p      | Differential operator                  |
| s      | Laplace operator                       |
| $X^c$  | Variable in the controller $dq0$ frame |
| $X^s$  | Variable in the system $dq0$ frame     |
| d      | Duty ratio                             |

## References

- Primadianto, A.; Lu, C.-N. A Review on Distribution System State Estimation. *IEEE Trans. Power Syst.* **2017**, *32*, 3875–3883. [[CrossRef](#)]
- Ahmad, F.; Rasool, A.; Ozsoy, E.; Sekar, R.; Sabanovic, A.; Elitaş, M. Distribution system state estimation—A step towards smart grid. *Renew. Sustain. Energy Rev.* **2018**, *81*, 2659–2671. [[CrossRef](#)]
- Cavvaro, G.; Arghandeh, R. Power distribution network topology detection with time-series signature verification method. *IEEE Trans. Power Syst.* **2018**, *33*, 3500–3509. [[CrossRef](#)]
- Zhou, X.; Tang, F.; Loh, P.C.; Jin, X.; Cao, W. Four-Leg Converters with Improved Common Current Sharing and Selective Voltage-Quality Enhancement for Islanded Microgrids. *IEEE Trans. Power Deliv.* **2016**, *31*, 522–531. [[CrossRef](#)]
- Hirve, S.; Chatterjee, K.; Fernandes, B.G.; Imayavaramban, M.; Dwari, S. PLL-Less Active Power Filter Based on One-Cycle Control for Compensating Unbalanced Loads in Three-Phase Four-Wire System. *IEEE Trans. Power Deliv.* **2007**, *22*, 2457–2465. [[CrossRef](#)]
- Morais, A.; Tofoli, F.L.; Barbi, I. Modeling, Digital Control, and Implementation of a Three-Phase Four-Wire Power Converter Used as A Power Redistribution Device. *IEEE Trans. Ind. Inf.* **2016**, *12*, 1035–1042. [[CrossRef](#)]
- Kerekes, T.; Teodorescu, R.; Liserre, M.; Klumpner, C.; Sumner, M. Evaluation of Three-Phase Transformerless Photovoltaic Inverter Topologies. *IEEE Trans. Power Electron.* **2009**, *24*, 2202–2211. [[CrossRef](#)]
- Pichan, M.; Rastegar, H. Sliding-Mode Control of Four-Leg Inverter with Fixed Switching Frequency for Uninterruptible Power Supply Applications. *IEEE Trans. Ind. Electron.* **2018**, *64*, 6805–6814. [[CrossRef](#)]

9. Carlos, G.; Jacobina, C.B.; Santos, E. Investigation on Dynamic Voltage Restorers with Two DC Links and Series Converters for Three-Phase Four-Wire Systems. *IEEE Trans. Ind. Appl.* **2016**, *52*, 1608–1620. [[CrossRef](#)]
10. Shukla, A.; Ghosh, A.; Joshi, A. Hysteresis current control operation of flying capacitor multilevel inverter and its application in shunt compensation of distribution systems. *IEEE Trans. Power Deliv.* **2007**, *22*, 396–405. [[CrossRef](#)]
11. Ramos-Carranza, H.A.; Medina, A.; Chang, G.W. Real-Time Shunt Active Power Filter Compensation. *IEEE Trans. Power Deliv.* **2008**, *23*, 2623–2625. [[CrossRef](#)]
12. Wandhare, R.G.; Agarwal, V. Reactive power capacity enhancement of a PV-grid system to increase PV penetration level in smart grid scenario. *IEEE Trans. Smart Grid.* **2014**, *5*, 1845–1854. [[CrossRef](#)]
13. Middlebrook, R.D. Measurement of loop gain in feedback systems. *Int. J. Electron.* **1975**, *38*, 485–512. [[CrossRef](#)]
14. Panov, Y.; Jovanovic, M.M. Stability and dynamic performance of current-sharing control for paralleled voltage regulator modules. *IEEE Trans. Power Electron.* **2002**, *17*, 172–179. [[CrossRef](#)]
15. Morroni, J.; Zane, R.; Maksimovic, D. An Online Stability Margin Monitor for Digitally Controlled Switched-Mode Power Supplies. *IEEE Trans. Power Electron.* **2009**, *24*, 2639–2648. [[CrossRef](#)]
16. Bottrell, N.; Prodanovic, M.; Green, T.C. Dynamic Stability of a Microgrid with an Active Load. *IEEE Trans. Power Electron.* **2013**, *28*, 5107–5119. [[CrossRef](#)]
17. Zeng, J.; Zhe, Z.; Qiao, W. An interconnection and damping assignment passivity-based controller for a DC–DC boost converter with a constant power load. *IEEE Trans. Ind. Appl.* **2014**, *50*, 2314–2322. [[CrossRef](#)]
18. Gu, Y.; Li, W.; He, X. Passivity-Based Control of DC Microgrid for Self-Disciplined Stabilization. *IEEE Trans. Power Syst.* **2015**, *30*, 2623–2632. [[CrossRef](#)]
19. Middlebrook, R.D. Input filter considerations in design and application of switching regulators. In Proceedings of the IEEE Industry Applications Society Annual Meeting, Chicago, IL, USA, 11–14 October 1976; pp. 94–107.
20. Sun, J. Small-signal methods for ac distributed power systems—A review. *IEEE Trans. Power Electron.* **2009**, *24*, 2545–2554.
21. Ren, Y.; Wang, X.; Chen, L.; Min, Y.; Li, G.; Wang, L.; Zhang, Y. A Strictly Sufficient Stability Criterion for Grid-Connected Converters Based on Impedance Models and Gershgorin’s Theorem. *IEEE Trans. Power Deliv.* **2020**, *35*, 1606–1609. [[CrossRef](#)]
22. Song, S.; Guan, P.; Liu, B.; Lu, Y.; Goh, H. Impedance Modeling and Stability Analysis of DFIG-Based Wind Energy Conversion System Considering Frequency Coupling. *Energies* **2021**, *14*, 3243. [[CrossRef](#)]
23. Xu, Y.; Nian, H.; Wang, Y.; Sun, D. Impedance Modeling and Stability Analysis of VSG Controlled Grid-Connected Converters with Cascaded Inner Control Loop. *Energies* **2020**, *13*, 5114. [[CrossRef](#)]
24. Cespedes, M.; Sun, J. Impedance Modeling and Analysis of Grid-Connected Voltage-Source Converters. *IEEE Trans. Power Electron.* **2014**, *29*, 1254–1261. [[CrossRef](#)]
25. Sun, J. Impedance-Based Stability Criterion for Grid-Connected Inverters. *IEEE Trans. Power Electron.* **2011**, *26*, 3075–3078. [[CrossRef](#)]
26. Rygg, A.; Molinas, M.; Zhang, C.; Cai, X. A Modified Sequence-Domain Impedance Definition and Its Equivalence to the dq-Domain Impedance Definition for the Stability Analysis of AC Power Electronic Systems. *IEEE J. Emerg. Sel. Top. Power Electron.* **2016**, *4*, 1383–1396. [[CrossRef](#)]
27. Nian, H.; Liao, Y.; Li, M.; Sun, D.; Xu, Y.; Hu, B. Impedance Modeling and Stability Analysis of Three-Phase Four-Leg Grid-Connected Inverter Considering Zero-Sequence. *IEEE Access* **2021**, *9*, 83676–83687. [[CrossRef](#)]
28. Hu, B.; Nian, H.; Yang, J.; Li, M.; Xu, Y. High-Frequency Resonance Analysis and Reshaping Control Strategy of DFIG System Based on DPC. *IEEE Trans. Power Electron.* **2021**, *36*, 7810–7819. [[CrossRef](#)]
29. Nian, H.; Yang, J.; Hu, B.; Jiao, Y.; Xu, Y.; Li, M. Stability Analysis and Impedance Reshaping Method for DC Resonance in VSCs-based Power System. *IEEE Trans. Energy Convers.* **2021**, *36*, 3344–3354. [[CrossRef](#)]